Supporting Information for

# Key Role of End-Capping Groups in Optoelectronic Properties of
# Poly-*p*-phenylene Cation Radicals

Marat R. Talipov, Anitha Boddeda, Qadir K. Timerghazin,* and Rajendra Rathore*

*Department of Chemistry*
*Marquette University*
*P.O. Box 1881, Milwaukee, WI 53201-1881 (USA)*
*Fax: (+1) 414-288-7066*
*E-mail: rajendra.rathore@marquette.edu, qadir.timerghazin@marquette.edu*

## Contents

## S1. Computational details

Electronic structure calculations were performed with the Gaussian 09 package, revision C01.[1] For density functional theory (DFT) calculations we used calibrated (see the next section for details) B1LYP functional[2] with 6-31G(d) basis set by Pople and co-workers.[3] Solvent effects were included using the implicit integral equation formalism polarizable continuum model (IEF-PCM)[4] with dichloromethane solvent parameters ($\varepsilon = 8.93$). In all DFT calculations, ultrafine Lebedev's grid was used with 99 radial shells per atom and 590 angular points in each shell For cation radicals $^{R}\mathbf{PP}_n^{+\bullet}$, wavefunction stability tests[5] was performed to ensure absence of solutions with lower energy. The values of $<S^2>$ operator after spin annihilation were confirmed to be close to the expectation value of 0.75. Unpaired spin density plots were rendered using isovalue of 0.001 a.u. Atomic charges were calculated using Natural Population Analysis approach,[6] a part of the Natural Bond Orbital analysis.[7] Energies of vertical electronic excitations and hole distribution in the first excited state of $^{R}\mathbf{PP}_n^{+\bullet}$ were computed using the time-dependent density functional theory (TD-DFT) method.[8] The one-particle density[9] was used to represent spatial distribution of the hole in first excited state. Tight cutoffs on forces and atomic displacement were used to determine convergence in geometry optimization procedure. Harmonic vibrational frequency calculations were performed for the optimized structures to confirm absence of imaginary frequencies. Free energies were computed within harmonic oscillator approximation for $T = 298.15$ K and $P = 1$ atm. In modeling the redox properties of the extended $^{R}\mathbf{PP}_n/^{R}\mathbf{PP}_n^{+\bullet}$ series ($n = 2$-10) only the electronic part of the oxidation free energies, $\Delta E^{\text{el}}$, have been used due to the emergence of highly anharmonic polymer-like vibrational modes in higher homologues ($n > 6$) that cannot be properly treated within the harmonic approximation used in our calculations (see Figure S9 and details in Section 3 below). Although the electronic energies of oxidation should not be directly compared with the experimental oxidation potentials, they allow study of the evolution of the electronic effects related to the hole stabilization across the entire $^{R}\mathbf{PP}_n^{+\bullet}$ series. In the DFT calculations, we used *iso*-propyl as a truncated model of the 6-tetradecyl (*iA*) end-capping substituent, and methoxy group as a truncated model of the 9-heptadecyloxy (*RO*) end-capping substituent.

## S2. Calibration of Computational Approach for $^{iA}PP_n/^{iA}PP_n^{+\bullet}$ Series

Delocalized π-conjugated cation radicals (CRs) such as $^RPP_n^{+\bullet}$ are challenging for many standard DFT methods due to the self-interaction error (SIE) problem[10] that causes artificial delocalization of the positive charge/hole.[11] This erroneous delocalization leads to increasingly underestimated oxidation potential for the longer chains and an incorrect nature of the first excited state of the CRs. The SIE can be reduced by using hybrid DFT methods that add a portion of the exact Hartree-Fock (HF) exchange term into the exchange functional.[12] However, the contribution of HF exchange in most of the widely used hybrid functionals, %HF < 30, is not sufficient for correct description of delocalized mixed-valence charged compounds; on the other hand, hybrid DFT functionals with %HF > 50 (global or long-range) often lead to over-localization of the charge/hole.[13] This necessitated fine-tuning of %HF for this class of delocalized CRs based on the available experimental data. Thus, we have calibrated[10b] a simple one-parameter density functional B1LYP[2] with respect to %HF against the experimental redox potentials and the lowest-energy optical transition energies in the $^{iA}PP_n/^{iA}PP_n^{+\bullet}$ series.[14] The resulting calibrated B1LYP functional with 40% of HF exchange (B1LYP-40) provides the best agreement with the experiment (Figure S1) when compared with several commonly used standard DFT functionals (CAM-B3LYP, M06-2X, ωB97X-D, Figures S2–S8). Importantly, the deviation of the $^{iA}PP_n^{+\bullet}$ oxidation potentials and excitation energies predicted by B1LYP-40 and obtained experimentally does not depend on the size of the system (i.e. slope ≈ 1), which suggests that the hole delocalization pattern in $^{iA}PP_n^{+\bullet}$ is computed correctly in every studied oligomer. Details of this calibration are presented below.
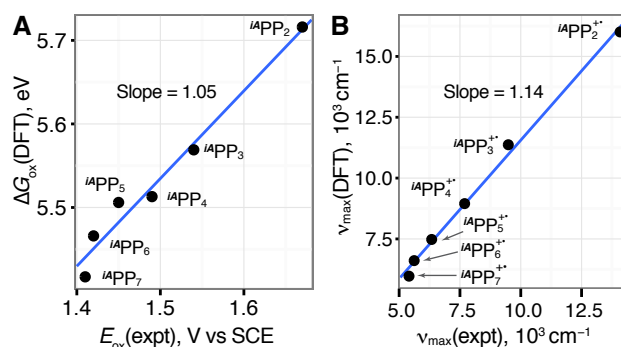


**Figure S1.** Comparison of experimental oxidation potentials of $^{iA}PP_2$–$^{iA}PP_7$ (A) and lowest-energy absorption maxima of $^{iA}PP_2^{+\bullet}$–$^{iA}PP_7^{+\bullet}$ (B) with the corresponding values calculated at the B1LYP-40/6-31G(d)+PCM (dichloromethane) level of theory.

In the benchmarking study, we employed several standard DFT functionals [BLYP,[15] B3LYP,[16] BHandHLYP (a.k.a. BHLYP),[1] CAM-B3LYP,[17] LC-BLYP,[15,18] M06-2X,[19] M06-HF,[20] ωB97X,[21] and ωB97X-D[22]]. Besides, we used modified B1LYP functional:[2]

$$E_{XC} = E_{XC}^{SVWN} + a_0(E_X^{exact} - E_X^{Slater}) + (1 - a_0)\Delta E_X^{B88} + \Delta E_C^{LYP} \qquad \text{(Eq. S1)}$$

where admixture of exact exchange $a_0$ varied from 20% to 50% with the step size of 5%. We used previously published experimental data a training set, which included oxidation potentials of $^{iA}PP_n$ and energies corresponding to $\lambda_{max}$ of the

electronic absorption spectra of $^{iA}PP_n$ and $^{iA}PP_n^{+\bullet}$, $n = 2$–7.[14] As none of these measured properties can be reproduced directly due to the presence of constant offsets that cannot be easily evaluated, we instead focused on finding a DFT functional that correctly reproduces the *evolution* of these properties in the $^{iA}PP_n$ series as function of $n$ so that the slope between experimental and calculated values is close to unity.

## S2.1. Oxidation potentials

We first investigated the performance of standard DFT methods, grouped by the form of their exchange-correlation functionals (Figure S2, Table S1), which showed that agreement with the experimental values depends on the amount of exact (Hartree-Fock-like) exchange in DFT methods. Low- or zero-HF functionals (%HF < 20), *viz.* BLYP and B3LYP, predict slope to be larger than unity, thus indicating artificial over-stabilization of $^{iA}PP_n^{+\bullet}$. In contrast, high-HF functionals (%HF > 50) result in the slope less than one, indicating that stability of $^{R}PP_n^{+\bullet}$ is underestimated by these methods. Figure S2A demonstrates that the slope gradually increases with the increasing %HF. Notably, correlation also becomes worse when %HF is increased beyond 50%. Interestingly, the CAM-B3LYP functional produces smaller error slope than BHLYP, thus demonstrating that the value of the slope in range-separated functionals mostly depends on the long-range %HF component, while being much less sensitive to the short-range %HF component.
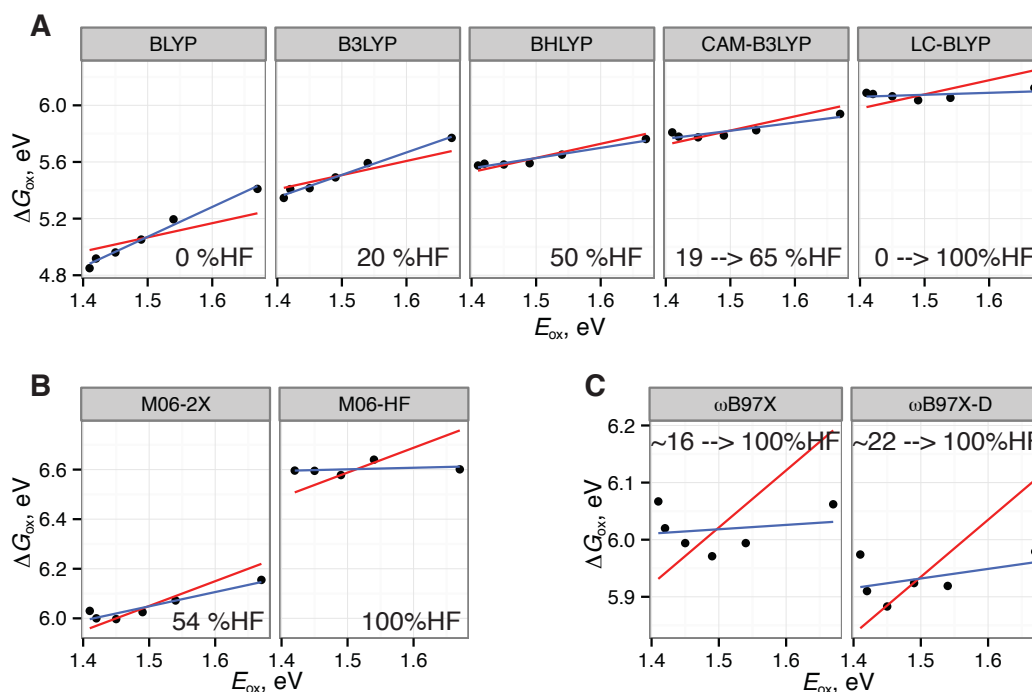


**Figure S2**. Comparison of the free energies of oxidation ($\Delta G_{ox}$), calculated by representative standard methods of the "B88$_x$ + LYP$_c$" (**A**), "M06" (**B**), and "$\omega$B97" (**C**) families of exchange-correlation functionals, against the measured oxidation potentials ($E_{ox}$) of $^{iA}PP_n$. Trend lines are shown in blue color. For convenience, 'ideal' cases with slope equal to unity are shown with red lines. For each DFT method, admixture of the exact Hartree-Fock-like functional is also shown (for range-separated functionals, short-range and long-range limit values are given).

**Table S1**. Free energies of oxidation ($\Delta G_{ox}$, eV), calculated by several standard DFT methods

| $n$ | BLYP | B3LYP | BHLYP | CAM-B3LYP | LC-BLYP | M06-2X | M06-HF | $\omega$B97X | $\omega$B97X-D | Expt [14] |
|---|---|---|---|---|---|---|---|---|---|---|
| 2 | 5.410 | 5.770 | 5.762 | 5.939 | 6.123 | 6.155 | 6.601 | 6.062 | 5.979 | 1.67 |
| 3 | 5.195 | 5.592 | 5.652 | 5.824 | 6.053 | 6.072 | 6.640 | 5.994 | 5.919 | 1.54 |
| 4 | 5.052 | 5.491 | 5.591 | 5.787 | 6.036 | 6.025 | 6.578 | 5.971 | 5.924 | 1.49 |
| 5 | 4.961 | 5.415 | 5.582 | 5.774 | 6.064 | 5.997 | 6.595 | 5.994 | 5.883 | 1.45 |
| 6 | 4.918 | 5.408 | 5.588 | 5.779 | 6.080 | 6.000 | 6.596 | 6.020 | 5.910 | 1.42 |
| 7 | 4.850 | 5.346 | 5.575 | 5.809 | 6.088 | 6.030 | - | 6.067 | 5.974 | 1.41 |

While most of the standard DFT functionals tested yielded non-unity slope, two functionals—B3LYP (20 %HF) and BHLYP (50 %HF)—gave the smallest deviation of the slope from unity. Because the slope obtained with B3LYP is slightly larger than 1.0, while the slope obtained with BHLYP is slightly lower than 1.0 (Figure S2A), the best correlation with the experimental data could be expected when using an exchange-correlation functional with %HF in the range from 20% to 50%. Thus, we tested the performance of a one-parameter B1LYP functional where we systematically varied %HF from 20% to 50% with a step size of 5%; further on, we refer to the resulting versions as B1LYP-20, B1LYP-25, *etc*. Comparison of the free energies of oxidation of $^{i4}PP_n$ with the corresponding oxidation potentials showed that the B1LYP-40 functional produces the slope closest to unity (Figure S3, Table S2).
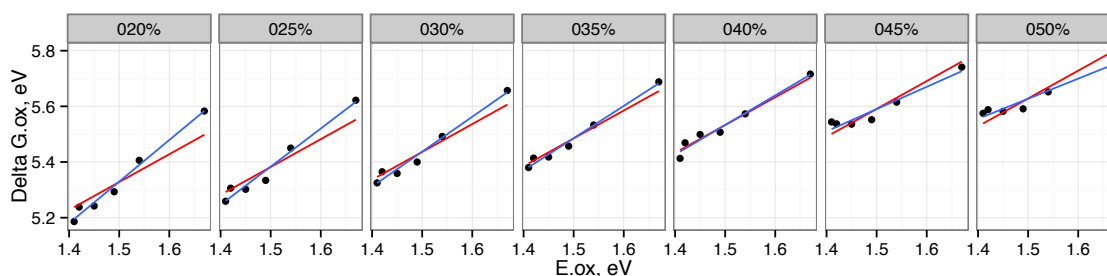


**Figure S3**. Comparison of the free energies of oxidation ($\Delta G_{ox}$), calculated by the series of modified B1LYP functionals with varied admixture of %HF (shown on the top of each panel), against the measured oxidation potentials ($E_{ox}$) of $^{i4}PP_n$. Trend lines are shown in blue color. For convenience, 'ideal' cases with slope equal to unity are shown with red lines.

**Table S2**. Free energies of oxidation ($\Delta G_{ox}$, eV), calculated the modified B1LYP functional with varied admixture of %HF

| $n$ | B1LYP-20 | B1LYP-25 | B1LYP-30 | B1LYP-35 | B1LYP-40 | B1LYP-45 | B1LYP-50 | Expt[14] |
|---|---|---|---|---|---|---|---|---|
| 2 | 5.583 | 5.622 | 5.657 | 5.688 | 5.716 | 5.741 | 5.762 | 1.67 |
| 3 | 5.406 | 5.450 | 5.492 | 5.533 | 5.573 | 5.615 | 5.652 | 1.54 |
| 4 | 5.293 | 5.334 | 5.400 | 5.457 | 5.507 | 5.552 | 5.591 | 1.49 |
| 5 | 5.242 | 5.302 | 5.359 | 5.418 | 5.499 | 5.536 | 5.582 | 1.45 |
| 6 | 5.238 | 5.306 | 5.365 | 5.414 | 5.469 | 5.537 | 5.588 | 1.42 |
| 7 | 5.186 | 5.259 | 5.325 | 5.380 | 5.413 | 5.544 | 5.575 | 1.41 |

## S2.2. Electronic excitation energies of $^{iA}\mathrm{PP}_n^{+\bullet}$

As in the case of the oxidation potentials, performance of standard DFT methods with respect to the electronic excitation energies in the $^{iA}\mathrm{PP}_n^{+\bullet}$ series depends on the amount of %HF exchange. Comparison of the calculated lowest-energy electronic transition energies in the $^{iA}\mathrm{PP}_n^{+\bullet}$ series with the wavenumbers corresponding to the experimental absorption maxima also shows a strong dependence of the performance of DFT method on the admixture of the HF-like term in the exchange functional (Figure S4, Table S3). None-/low-HF functionals (*viz.* BLYP, B3LYP) result in a concaved-down trend curve, whereas the ωB97X-D functional, which has 100%-HF long-range term, results in a concaved-up trend curve. At the same time, DFT methods with %HF ~ 50–60 (in particular, CAM-B3LYP, M06-2X, and, slightly worse, BHLYP) provide the straight trend line with $R^2$ close to unity, and with the slope also close to unity.
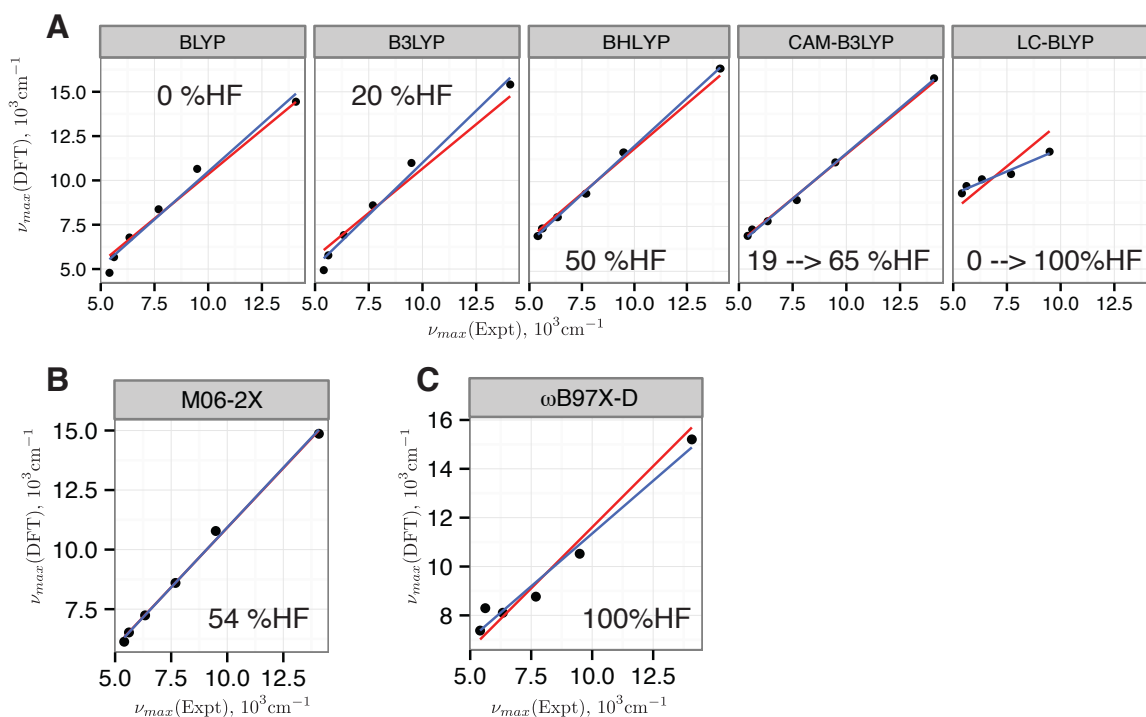


**Figure S4**. Comparison of the excitation energies of the lowest-energy optical transitions calculated by some representative standard methods of the "B88$_x$ + LYP$_c$" (**A**), "M06" (**B**), and "ωB97" (**C**) families of exchange-correlation functionals, against the energies corresponding to the $\lambda_{max}$ obtained from the electronic absorption spectra of $^{iA}\mathrm{PP}_n^{+\bullet}$. Trend lines are shown in blue color. For convenience, 'ideal' cases with slope equal to unity are shown with red lines. For each DFT method, admixture of the exact Hartree-Fock-like functional is also shown (for range-separated functionals, short-range and long-range limit values are given).

**Table S3.** Excitation energies (cm$^{-1}$) of the lowest-energy optical transitions of $^{iA}\mathbf{PP}_n^{+\bullet}$, calculated by means of some representative standard exchange-correlation functionals

| $n$ | BLYP | B3LYP | BHLYP | CAM-B3LYP | LC-BLYP | M06-2X | wB97X-D |
|---|---|---|---|---|---|---|---|
| 2 | 14440 | 15411 | 16302 | 15760 | - | 14863 | 15204 |
| 3 | 10650 | 10984 | 11626 | 11016 | 11622 | 10781 | 10522 |
| 4 | 8371 | 8593 | 9328 | 8890 | 10360 | 8601 | 8766 |
| 5 | 6779 | 6913 | 8016 | 7697 | 10064 | 7239 | 8107 |
| 6 | 5671 | 5773 | 7388 | 7231 | 9682 | 6522 | 8295 |
| 7 | 4786 | 4937 | 6966 | 6870 | 9271 | 6132 | 7378 |

Then, we explored role of %HF using series of the B1LYP-XX functionals in the same manner as it was done in the previous section. In accord with the results obtained for the standard DFT methods, the slope of the trend line gradually decreases from B1LYP-20 to B1LYP-50, with the slope closest to unity in the latter case (Figure S5, Table S4).
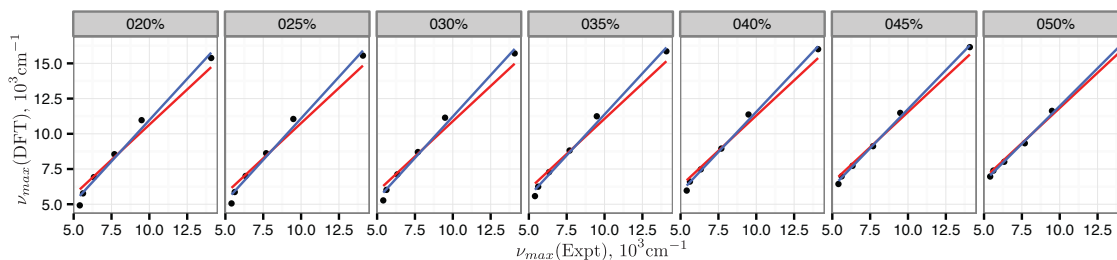


**Figure S5**. Comparison of the excitation energies of the lowest-energy optical transitions, calculated by the series of modified B1LYP functionals with varied admixture of %HF (shown on the top of each panel), with the energies corresponding to the $\lambda_{max}$ obtained from the electronic absorption spectra of $^{iA}\mathbf{PP}_n^{+\bullet}$. Trend lines are shown in blue color. For convenience, 'ideal' cases with slope equal to unity are shown with red lines. For each DFT method, admixture of the exact Hartree-Fock-like functional is also shown (for range-separated functionals, short-range and long-range limit values are given).

**Table S4.** Excitation energies (cm$^{-1}$) of the lowest-energy optical transitions of $^{iA}\mathbf{PP}_n^{+\bullet}$, calculated by the series of modified B1LYP functionals with varied admixture of %HF

| $n$ | B1LYP-20 | B1LYP-25 | B1LYP-30 | B1LYP-35 | B1LYP-40 | B1LYP-45 | B1LYP-50 | Expt [14] |
|---|---|---|---|---|---|---|---|---|
| 2 | 15383 | 15553 | 15710 | 15860 | 16007 | 16153 | 16302 | 14085 |
| 3 | 10969 | 11052 | 11143 | 11244 | 11370 | 11484 | 11626 | 9488 |
| 4 | 8552 | 8620 | 8705 | 8813 | 8951 | 9122 | 9328 | 7692 |
| 5 | 6923 | 7004 | 7121 | 7279 | 7478 | 7727 | 8016 | 6337 |
| 6 | 5770 | 5867 | 6019 | 6246 | 6608 | 6979 | 7388 | 5618 |
| 7 | 4918 | 5057 | 5271 | 5576 | 5969 | 6436 | 6966 | 5405 |

## S2.3. Electronic excitation energies of $^{iA}PP_n$

Although we focused discussion on the $^{R}PP_n^{+\bullet}$ rather than on their uncharged counterparts, the latter can provide additional data for benchmarking and tuning the DFT functional. Here, we employ this information by comparing ability of the DFT methods to reproduce experimental $\lambda_{max}$ corresponding the lowest-energy electronic transition.

Comparison of the calculated lowest-energy electronic transition energies in $^{iA}PP_n$ with the wavenumbers corresponding to the experimental absorption maxima also shows a strong dependence of the performance of DFT method on the admixture of the HF-like term in the exchange functional (Figure S6, Table S5). Low-/none-HF functionals (viz. BLYP, B3LYP) result in a trend line slope larger than unity, indicating that they systematically overstabilize the excited state with respect to increasing number of $p$-phenylene units. In opposite, the slope of the trend line is less then unity for the high-HF DFT (permanent or long-range %HF = 100) methods. At the same time, DFT methods with %HF ~ 50–60 (BHLYP, CAM-B3LYP, M06-2X) perform best in this case.
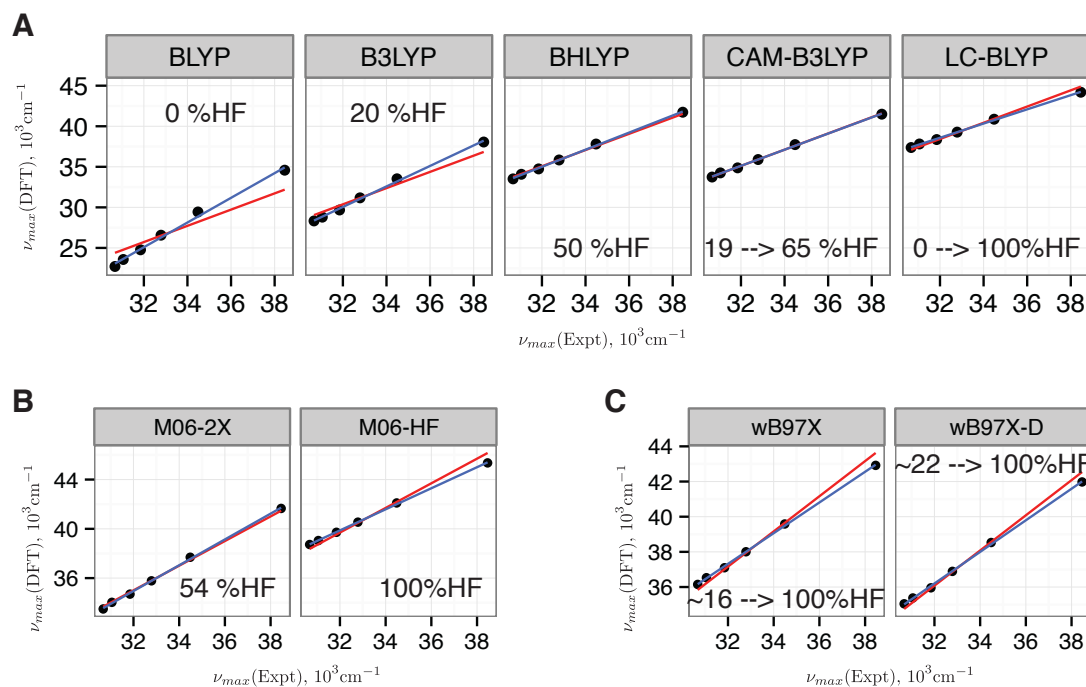
**Figure S6**. Comparison of the excitation energies of the lowest-energy optical transitions, calculated by some representative standard methods of the "B88$_x$ + LYP$_c$" (**A**), "M06" (**B**), and "$\omega$B97" (**C**) families of exchange-correlation functionals, with the energies corresponding to the $\lambda_{max}$ obtained from the electronic absorption spectra of $^{iA}PP_n$. Trend lines are shown in blue color. For convenience, 'ideal' cases with slope equal to unity are shown with red lines. For each DFT method, admixture of the exact Hartree-Fock-like functional is also shown (for range-separated functionals, short-range and long-range limit values are given).

**Table S5.** Excitation energies (cm$^{-1}$) of the lowest-energy optical transitions of $^{i4}$**PP**$_n$, calculated by several DFT methods

| $n$ | BLYP | B3LYP | BHLYP | CAM-B3LYP | LC-BLYP | M06-2X | M06-HF | $\omega$B97X | $\omega$B97X-D | Expt[14] |
|---|---|---|---|---|---|---|---|---|---|---|
| 2 | 34584 | 38056 | 41731 | 41489 | 44193 | 41655 | 45351 | 42918 | 41976 | 38462 |
| 3 | 29435 | 33523 | 37809 | 37737 | 40868 | 37693 | 42100 | 39585 | 38531 | 34483 |
| 4 | 26569 | 31174 | 35844 | 35898 | 39276 | 35778 | 40542 | 38005 | 36891 | 32787 |
| 5 | 24770 | 29679 | 34743 | 34871 | 38360 | 34698 | 39717 | 37097 | 35956 | 31847 |
| 6 | 23576 | 28795 | 34077 | 34251 | 37814 | 34033 | 39049 | 36530 | 35378 | 31056 |
| 7 | 22714 | 28328 | 33513 | 33738 | 37376 | 33495 | 38727 | 36148 | 35047 | 30675 |

Then, we explored role of %HF using series of the B1LYP-XX functionals in the same manner as it was done in the previous sections. In accord with the results obtained for the standard DFT methods, the slope of the trend line gradually decreases from B1LYP-20 to B1LYP-50, with the slope closest to unity in the latter case (Figure S7, Table S6).



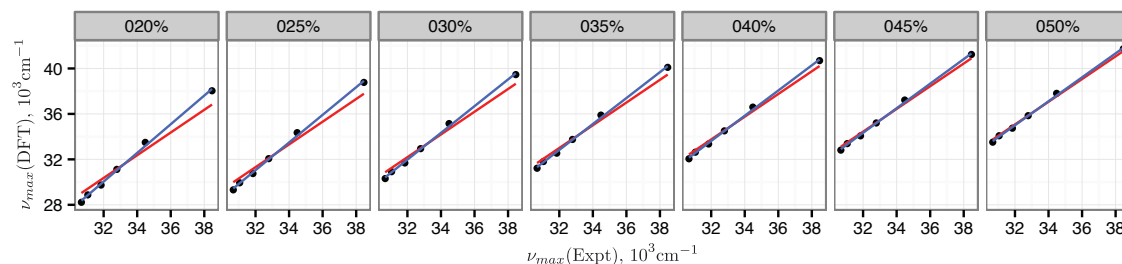**Figure S7**. Comparison of the excitation energies of the lowest-energy optical transitions, calculated by the series of modified B1LYP functionals with varied admixture of %HF (shown on the top of each panel), with the energies corresponding to the $\lambda_{max}$ obtained from the electronic absorption spectra of $^{i4}$**PP**$_n$. Trend lines are shown in blue color. For convenience, 'ideal' cases with slope equal to unity are shown with red lines. For each DFT method, admixture of the exact Hartree-Fock-like functional is also shown (for range-separated functionals, short-range and long-range limit values are given).

**Table S6.** Excitation energies (cm$^{-1}$) of the lowest-energy optical transitions of $^{i4}$**PP**$_n$, calculated by the series of modified B1LYP functionals with varied admixture of %HF

| $n$ | B1LYP-20 | B1LYP-25 | B1LYP-30 | B1LYP-35 | B1LYP-40 | B1LYP-45 | B1LYP-50 | Expt[14] |
|---|---|---|---|---|---|---|---|---|
| 2 | 38037 | 38773 | 39460 | 40098 | 40690 | 41234 | 41731 | 38462 |
| 3 | 33494 | 34351 | 35149 | 35894 | 36598 | 37220 | 37809 | 34483 |
| 4 | 31118 | 32063 | 32940 | 33753 | 34507 | 35203 | 35844 | 32787 |
| 5 | 29738 | 30749 | 31683 | 32544 | 33351 | 34069 | 34743 | 31847 |
| 6 | 28873 | 29938 | 30915 | 31811 | 32632 | 33386 | 34077 | 31056 |
| 7 | 28221 | 29316 | 30310 | 31219 | 32050 | 32813 | 33513 | 30675 |

## S2.4. Conclusions from the benchmarking studies

In total, we found that pure or low-%HF density functionals tend to overestimate stabilization of the $^R\mathrm{PP}_n^{+\bullet}$ due to artificial delocalization of the hole. In opposite, high-%HF density functionals tend to underestimate stabilization of $^R\mathrm{PP}_n^{+\bullet}$ due to artificially compact localization of the hole, which might even reside only one monomer unit. In both extremes, we found not very good agreement of the evolution of oxidation and vertical excitation energies in $^{iA}\mathrm{PP}_n/^{iA}\mathrm{PP}_n^{+\bullet}$ when compared with experiment. On the other hand, a more balanced description might be provided by density functionals with intermediate admixture of HF-like term, %HF = 20–50% (Figure S8, Tables S7 and S8).
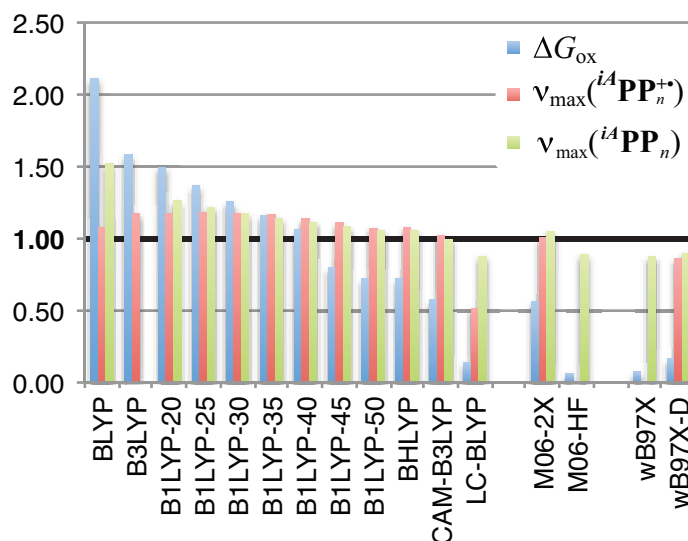


**Figure S8**. Overall comparison of the slopes of trend lines of vertical electronic excitation energies of $^{iA}\mathrm{PP}_n/^{iA}\mathrm{PP}_n^{+\bullet}$, and oxidation energies of $^{iA}\mathrm{PP}_n$.

**Table S7**. Slopes of trend lines (DFT vs experiment) of vertical excitation energies of $^{iA}\mathrm{PP}_n/^{iA}\mathrm{PP}_n^{+\bullet}$, and free energies of oxidation of $^{iA}\mathrm{PP}_n$, $n = 2$–7

| DFT | %HF | $\nu_{max}(^{iA}\mathrm{PP}_n)$, cm$^{-1}$ | $\nu_{max}(^{iA}\mathrm{PP}_n^{+\bullet})$, cm$^{-1}$ | $\Delta G_{ox}$, eV |
|---|---|---|---|---|
| BLYP | - | 1.52 | 1.08 | 2.11 |
| B3LYP | 20 | - | 1.17 | 1.58 |
| B1LYP-20 | 20 | 1.26 | 1.17 | 1.49 |
| B1LYP-25 | 25 | 1.22 | 1.18 | 1.37 |
| B1LYP-30 | 30 | 1.18 | 1.18 | 1.25 |
| B1LYP-35 | 35 | 1.14 | 1.16 | 1.16 |
| B1LYP-40 | 40 | 1.11 | 1.14 | 1.06 |
| B1LYP-45 | 45 | 1.08 | 1.11 | 0.80 |
| B1LYP-50 | 50 | 1.05 | 1.07 | 0.72 |

| DFT | %HF | $\nu_{max}(^{iA}\mathbf{PP}_n)$, cm$^{-1}$ | $\nu_{max}(^{iA}\mathbf{PP}_n^{+\bullet})$, cm$^{-1}$ | $\Delta G_{ox}$, eV |
|---|---|---|---|---|
| BHLYP | 50 | 1.05 | 1.08 | 0.72 |
| CAM-B3LYP | 19–65 | 1.00 | 1.02 | 0.57 |
| LC-BLYP | 0–100 | 0.88 | 0.52 | 0.14 |
| M06-2X | 54 | 1.05 | 1.00 | 0.57 |
| M06-HF | 100 | 0.89 | - | 0.06 |
| ωB97X | 16–100 | 0.87 | - | 0.08 |
| ωB97X-D | 22–100 | 0.90 | 0.86 | 0.17 |

**Table S8**. Correlation coefficients of the DFT vs experimental trend lines corresponding to the vertical excitation energies of $^{iA}\mathbf{PP}_n$ and $^{iA}\mathbf{PP}_n^{+\bullet}$, and free energies of oxidation of $^{iA}\mathbf{PP}_n$, $n = 2–7$

| DFT | %HF | $\nu_{max}(^{iA}\mathbf{PP}_n)$ | $\nu_{max}(^{iA}\mathbf{PP}_n^{+\bullet})$ | $\Delta G_{ox}$ |
|---|---|---|---|---|
| BLYP | - | 0.9917 | 0.9714 | 0.9814 |
| B3LYP | 20 | 0.9964 | 0.9823 | 0.9818 |
| B1LYP-20 | 20 | 0.9969 | 0.9820 | 0.9794 |
| B1LYP-25 | 25 | 0.9974 | 0.9846 | 0.9639 |
| B1LYP-30 | 30 | 0.9977 | 0.9876 | 0.9721 |
| B1LYP-35 | 35 | 0.9979 | 0.9910 | 0.9834 |
| B1LYP-40 | 40 | 0.9980 | 0.9941 | 0.9628 |
| B1LYP-45 | 45 | 0.9982 | 0.9968 | 0.9171 |
| B1LYP-50 | 50 | 0.9983 | 0.9981 | 0.9245 |
| BHLYP | 50 | 0.9983 | 0.9973 | 0.9245 |
| CAM-B3LYP | 19–65 | 0.9987 | 0.9973 | 0.7695 |
| LC-BLYP | 0–100 | 0.9989 | 0.9423 | 0.0003 |
| M06-2X | 54 | 0.9989 | 0.9956 | 0.8578 |
| M06-HF | 100 | 0.9994 | - | -0.2371 |
| ωB97X | 16–100 | 0.9992 | - | -0.2053 |
| ωB97X-D | 22–100 | 0.9991 | 0.9658 | -0.0144 |

To find the optimal amount of exact exchange, we followed procedure suggested by Lambert and Kaupp [10b] that involves systematic scanning of %HF in the B1LYP functional. Rather than trying to reproduce absolute values of experimentally obtained optoelectronic properties of $^{iA}\mathbf{PP}_n/^{iA}\mathbf{PP}_n^{+\bullet}$, we aimed to find a DFT functional that correctly reproduces *evolution* of these properties in oligomer series $^{R}\mathbf{PP}_n$ as function of $n$, i.e. keeps the slope between experimental and calculated values, equal to unity. The slopes of the trend lines, corresponding to the excitation energies of both neutral and cation radical $^{iA}\mathbf{PP}_n$, are close to unity for %HF in the range from 35% (B1LYP-35) to 50% (B1LYP-50) to ~65% (long-range HF-component of CAM-B3LYP), with the best results achieved for CAM-B3LYP functional. However, CAM-B3LYP

cannot properly reproduce evolution of the oxidation energies of $^{i4}\text{PP}_n$, which can be seen from the small slope of the trend line (0.57) and low $R^2$ coefficient, 0.75. At the same time, the best agreement to experimental oxidation potentials can be achieved by using the B1LYP functional with 40% of exact exchange, B1LYP-40, which has a slope of 1.06 and $R^2 = 0.96$. Notably, even little increase of %HF leads to the significant performance degradation: for B1LYP-45, slope is 0.80, and $R^2$ reduces to 0.92. Therefore, the B1LYP functional with 40% admixture of the HF-like term, B1LYP-40, is the functional that provides the best overall agreement with the experimentally observed evolutions of optoelectronic properties of $^{i4}\text{PP}_n/^{i4}\text{PP}_n^{+\bullet}$ with respect to increasing number of monomer units $n$.

## S3. Issues with evaluation of thermodynamic functions in $^{R}PP_{n}^{+\bullet}$

Although the calculated free energies of oxidation of $^{iA}PP_2–^{iA}PP_7$ are highly consistent with the experimental oxidation potentials (Figure S1A, S2, and S3), further expansion of the series resulted in significant numerical noise in the calculated enthalpy and, especially, entropy functions. This noise arises from the uncertainty in the calculations of low-frequency (<10 cm$^{-1}$) vibrational modes, which render emerging polymer behavior of $^{iA}PP_n^{+\bullet}$. The problem with numerical noise persisted after tightening threshold for geometry optimization, increasing the integration grid quality, and increasing energy/gradient accuracy. The numerical noise was observed for all applied DFT methods (see Figure S9), showing magnitude within ~50 meV, which still allows reasonable comparison with the experimental oxidation potentials, but hinders analysis of fine details of the evolution of oxidation energies of $^{iA}PP_n$ in longer oligomer series, $n \geq 8$. Thus, we analyzed only the electronic part of the oxidation energy $\Delta E^{el}$, although this quantity, unlike free energy of oxidation, can be expected to correlate less well with the measured oxidation potentials $E_{ox}$. However, comparison of the evolution of calculated $\Delta E^{el}$ and experimental $E_{ox}$ values (Figures 2A and 3A in the main text) shows a very good agreement.
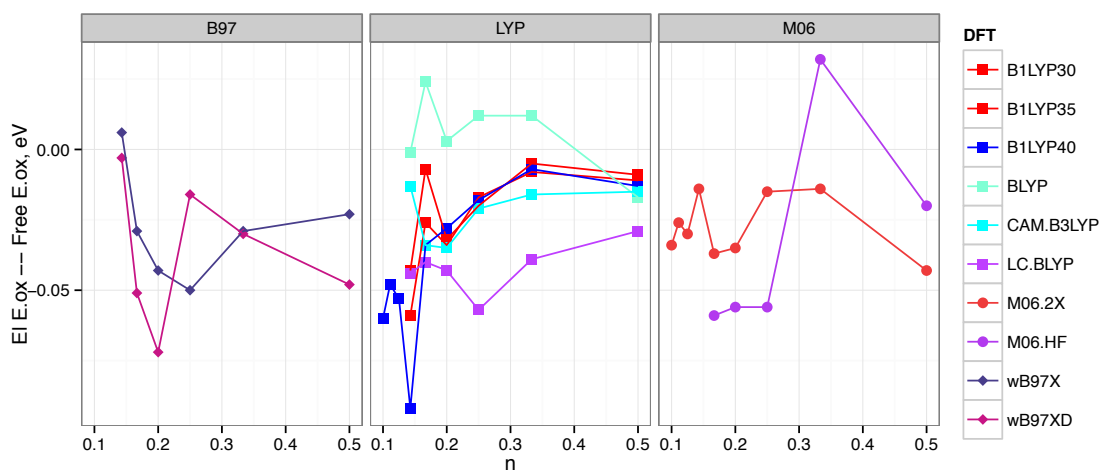


**Figure S9**. Contribution of the thermodynamic functions in the oxidation energies of $^{iA}PP_n$ (i.e. $\Delta E^{el} – \Delta G_{ox}$), calculated by means of different DFT methods.

## S4. Comparison of redox and spectroscopic properties of helical and alternant conformers of $^R$PP$_n$/$^R$PP$_n^{+\bullet}$

We found that neutral $^R$PP$_n$ are more stable by ~0.1 kcal/mol in the alternant conformation, where all the next nearest neighbors are eclipsed (Table S9). At the same time, $^R$PP$_n^{+\bullet}$ are more stable by up to ~0.3 kcal/mol in the helical conformation.
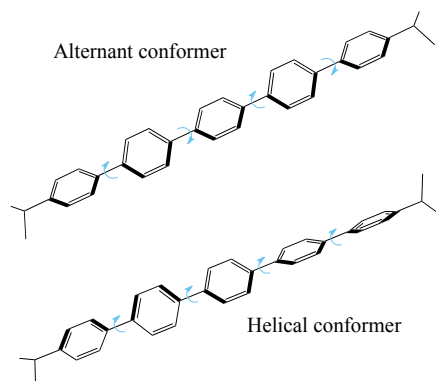


In the main text, we present data for the most stable conformer in each case; however, this choice does not significantly affect results, as alternant and helical $^R$PP$_n$, either in neutral or cation radicals form, show very similar properties (Figure S10). The unpaired spin distribution in alternant and helical conformers of $^R$PP$_n^{+\bullet}$ is also nearly identical (Figure S11).
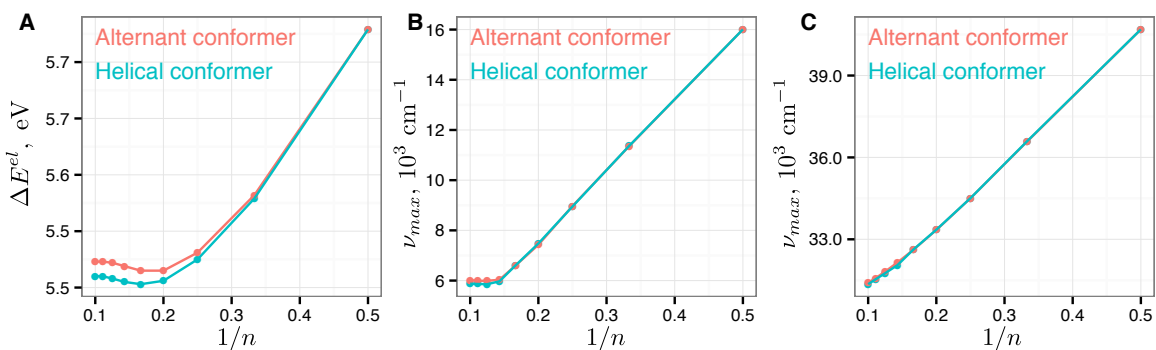


**Figure S10**. Comparison of the electronic energies of oxidation (**A**), electronic excitation energies of the cation radical (**B**) and neutral (**C**) forms of the helical and alternant conformers of the $^{iA}$PP$_n$ molecules, calculated at the B1LYP-40/6-31G(d)+PCM (dichloromethane) level of theory.
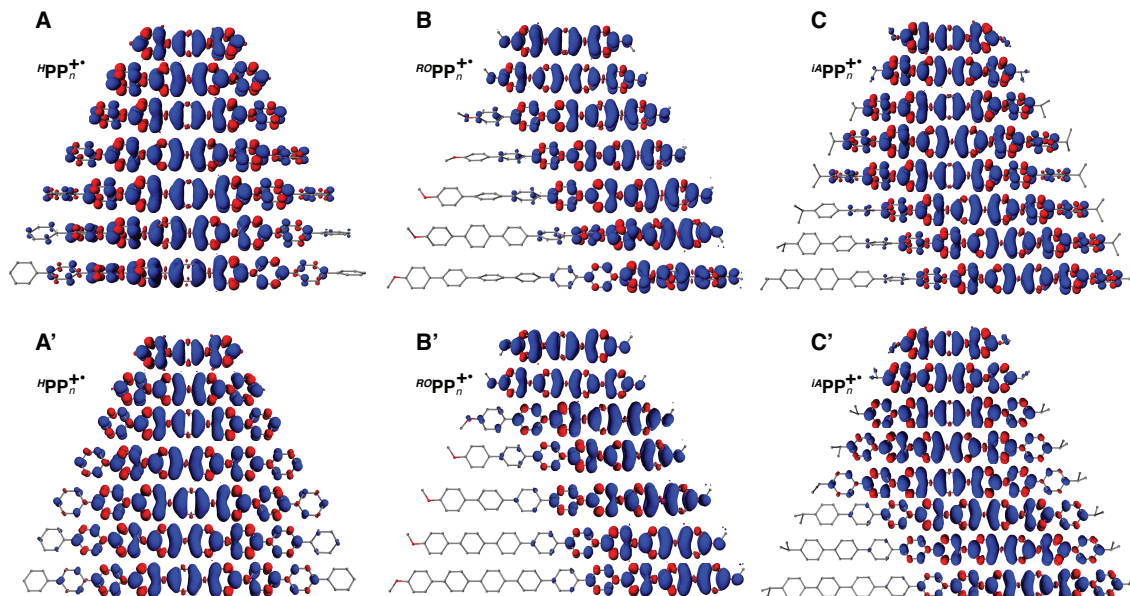
**Figure S11**. Isosurface plots of the unpaired spin density in the ground state of helical (**A–C**) and alternant (**A'–C'**) conformers of $^{R}\mathbf{PP}_{n}^{+\bullet}$, calculated at the B1LYP-40/6-31G(d)+PCM(dichloromethane) level of theory.

**Table S9**. Relative electronic energies (in kcal/mol) of alternant and helical conformers in the $^{R}\mathbf{PP}_{n}/^{R}\mathbf{PP}_{n}^{+\bullet}$ series (positive values correspond to higher energy of alternant conformer) , calculated at the B1LYP-40/6-31G(d)+PCM(dichloromethane) level of theory.

| $n$ | $^{H}\mathbf{PP}_{n}$ | | $^{RO}\mathbf{PP}_{n}$ | | $^{iA}\mathbf{PP}_{n}$ | |
|---|---|---|---|---|---|---|
| | CR | N | CR | N | CR | N |
| 3 | 0.03 | -0.04 | 0.02 | -0.06 | 0.03 | -0.04 |
| 4 | 0.07 | -0.07 | 0.08 | -0.08 | 0.07 | -0.06 |
| 5 | 0.11 | -0.10 | 0.10 | -0.12 | 0.10 | -0.10 |
| 6 | 0.14 | -0.13 | 0.06 | -0.15 | 0.14 | -0.16 |
| 7 | 0.10 | -0.18 | 0.00 | -0.19 | 0.14 | -0.17 |
| 8 | 0.14 | -0.20 | - | -0.22 | 0.13 | -0.20 |
| 9 | 0.14 | -0.23 | 0.00 | -0.25 | 0.08 | -0.23 |
| 10 | - | -0.27 | - | -0.29 | 0.05 | -0.25 |

Scheme S1.
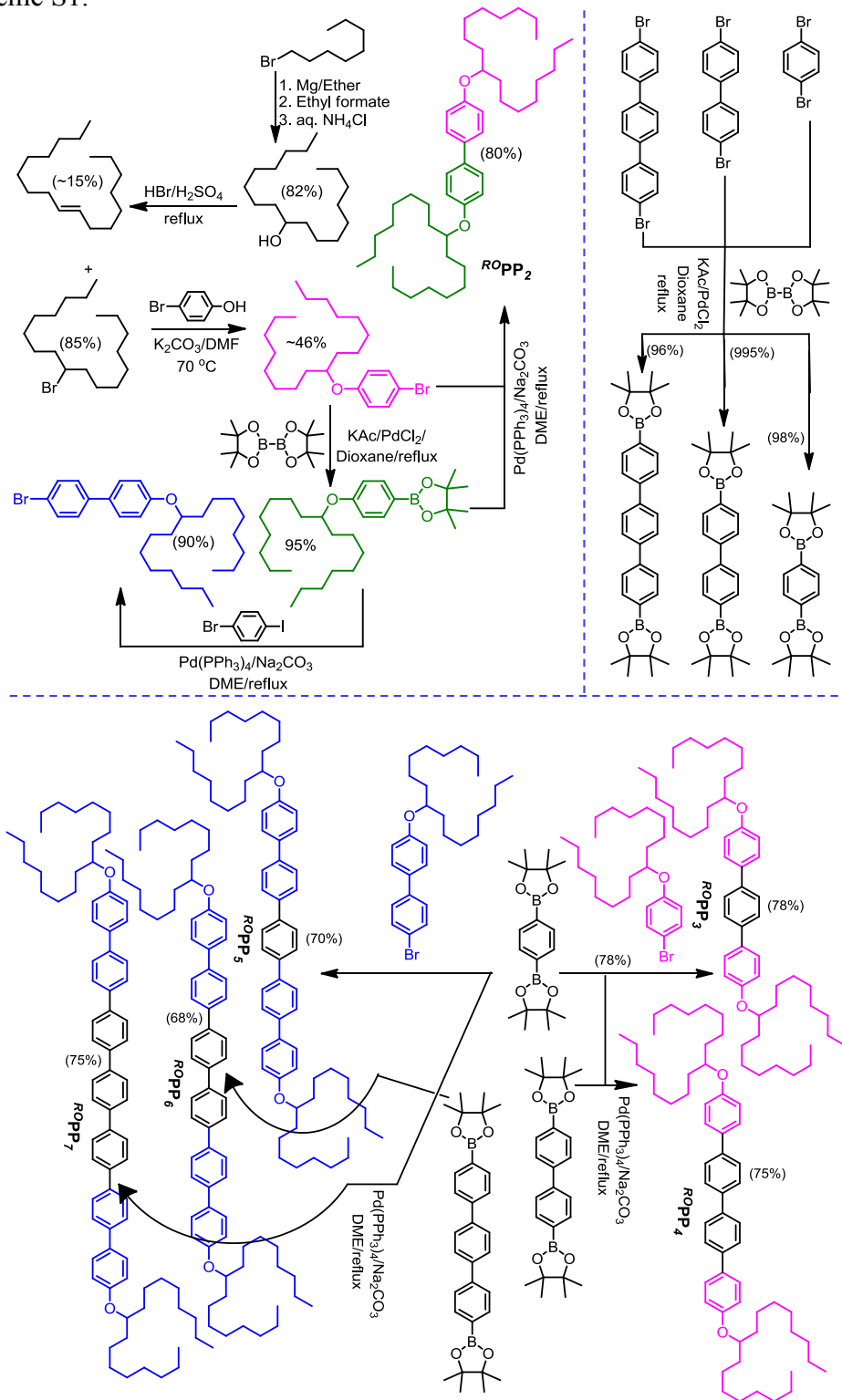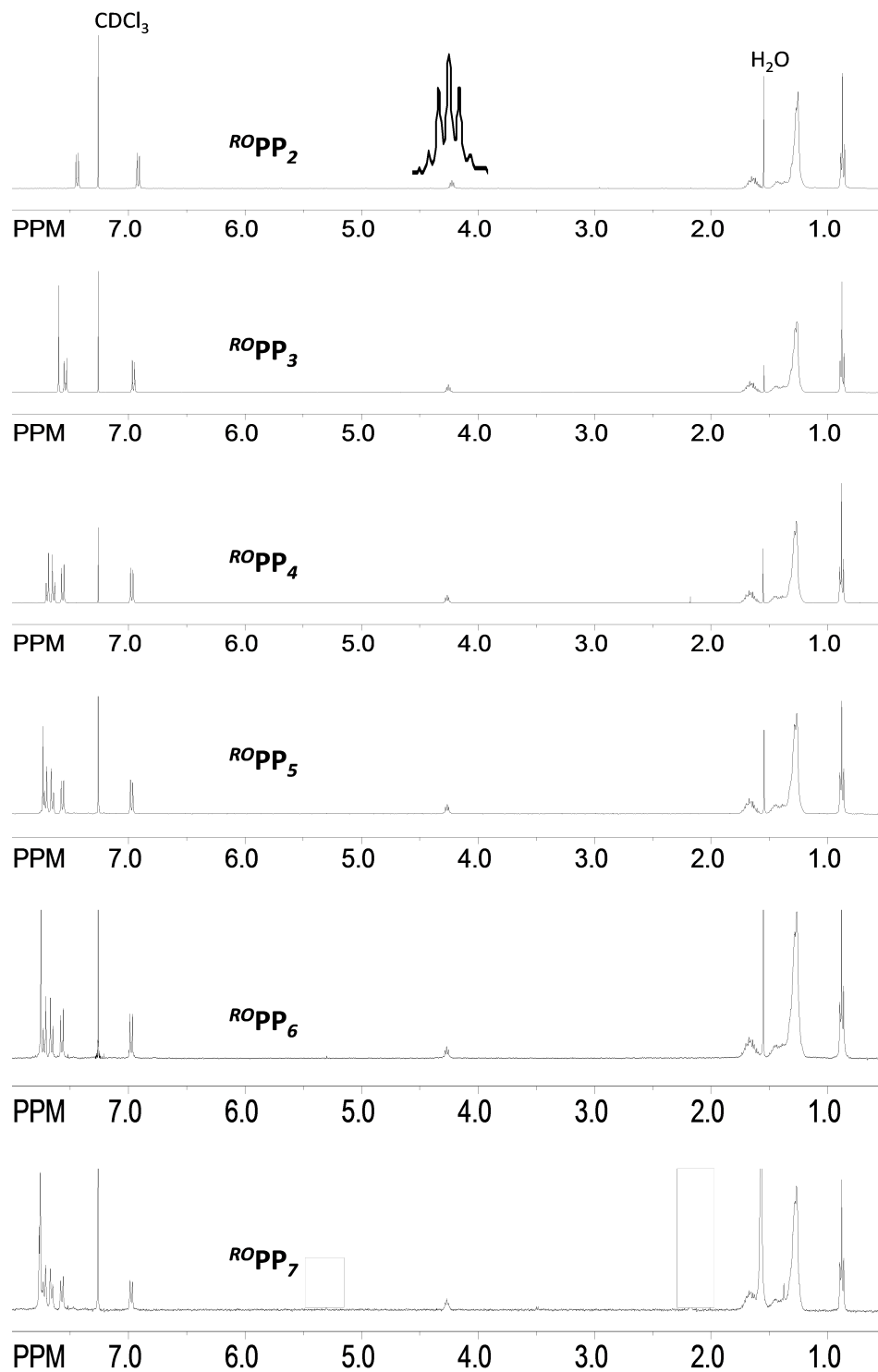
**Figure S12.** The $^1$H NMR spectra of various $^{RO}$PP$_n$ oligomers recorded in CDCl$_3$ at 22 $^o$C.
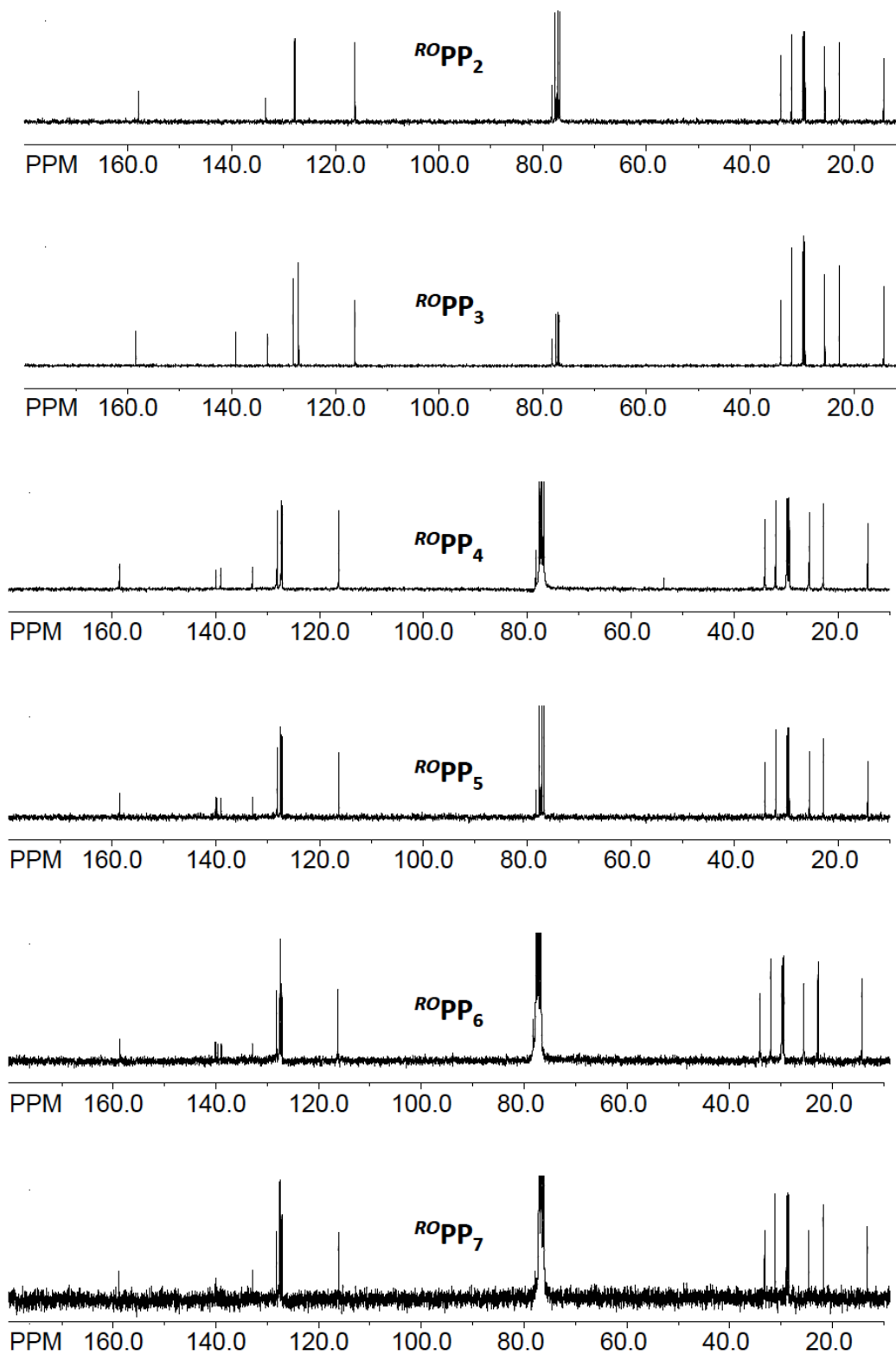
**Figure S13.** The $^{13}$C NMR spectra of various $^{RO}PP_n$ oligomers recorded in CDCl$_3$ at 22 $^o$C
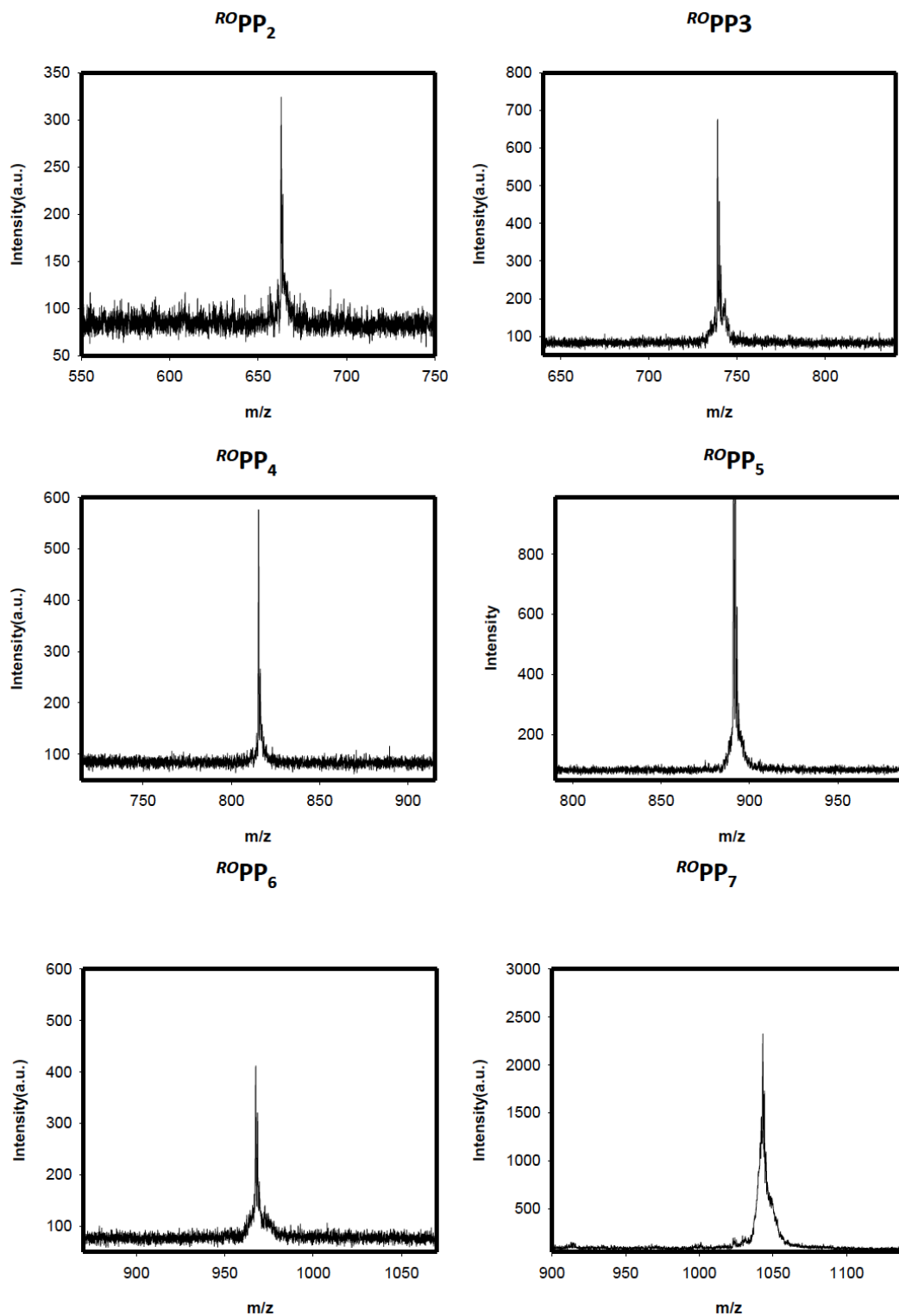
**Figure S14.** The MALDI mass-spectra of various $^{RO}PP_n$ oligomers recorded in 9-nitroanthracene matrix. The spectra were truncated to remove peaks due to matrix for clarity.
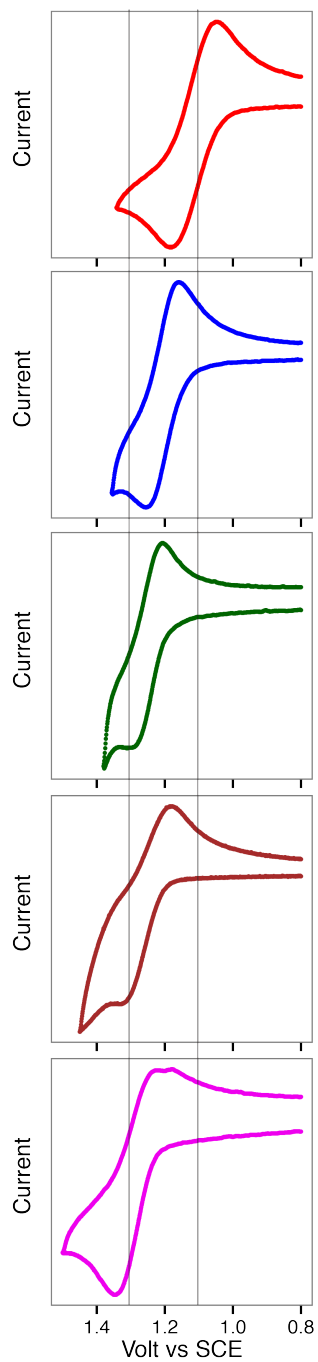
**Figure S15.** Cyclic voltammograms of 0.1 mM $^{RO}\mathbf{PP}_n$ in $CH_2Cl_2$ containing 0.1 M tetra-*n*-butylammonium hexafluorophosphate (*n*-Bu$_4$NPF$_6$) as the supporting electrolyte at a scan rate 200 mV/sec at 22° C.

**Table S10**. Oxidation potentials of $^{RO}PP_n$ and optical properties of the corresponding cation radicals

| $^{RO}PP_n$ $n = \ldots$ | $E_{ox1}$ vs SCE | $^{RO}PP_n^{+\bullet}$ $\lambda_{max}$ | $^{RO}PP_n^{+\bullet}$ $\nu_{max}$ | $^{RO}PP_n^{+\bullet}$ $\varepsilon_{max}$ |
|---|---|---|---|---|
| | V | nm | cm$^{-1}$ | M$^{-1}$ cm$^{-1}$ |
| 2 | 1.19 | 832 | 12019 | 12100 |
| 3 | 1.25 | 1210 | 8264 | 31300 |
| 4 | 1.28 | 1596 | 6266 | 33400 |
| 5 | 1.30 | 1520 | 6759 | 15000 |
| 6 | 1.31 | 1402 | 7133 | 14200 |
| 7 | 1.31 | 1400 | 7143 | ~7000 |

The observed evolution of the experimental $E_{ox}$ values of $^{RO}PP_n$ (Table S10 and Figure 3A in the main text) show an excellent agreement with computational predictions (Figure 1A in the main text) and reveal drastic differences from the previously reported $E_{ox}$ values for the $^{iA}PP_n$ series. Indeed, addition of each *p*-phenylene unit leads to a linear increase vs $1/n$ of the oxidation potential in $^{RO}PP_n$. Clearly, this finding suggests that a substitution of the *iso*-alkyl end-capping group by the *iso*-alkoxy group causes significant changes in the electronic structure of $^{RO}PP_n^{+\bullet}$.

The electrochemical reversibility and relatively low oxidation potentials of $^{RO}PP_n$ allowed synthesizing the corresponding cation radicals $^{RO}PP_n^{+\bullet}$ in a reaction with naphthalene cation radical ($NAP^{+\bullet}$),[23] a robust one-electron oxidant ($E_{ox}$ = 1.34 V vs. SCE). Figure 2 in the main text shows the spectral changes attendant upon the reduction of a 0.1 mM solution of $NAP^{+\bullet}$ ($\lambda_{max}$ = 672, 616, 503, and 396 nm; $\varepsilon_{672}$ = 9300 M$^{-1}$ cm$^{-1}$) [23] and oxidation of $^{RO}PP_2$ to its cation radical $^{RO}PP_2^{+\bullet}$ ($\lambda_{max}$ = 832 nm) by an incremental addition of $^{RO}PP_2$ in dichloromethane at 22 °C. The presence of a clear isosbestic point at $\lambda_{max}$ = 691 nm in Figure S16A establishes the uncluttered nature of electron transfer from $^{RO}PP_2$ to $NAP^{+\bullet}$:
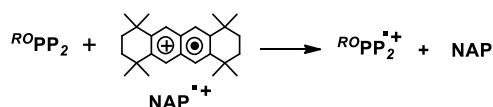


Furthermore, a plot of the depletion of $NAP^{+\bullet}$ (i.e. the decrease of the absorbance at 672 nm) and formation of $^{RO}PP_2^{+\bullet}$ (i.e. an increase in the absorbance at 832 nm) against the increments of added $^{RO}PP_2$ (Figure 2B), established that $NAP^{+\bullet}$ was completely consumed after the addition of 1 equiv. of $^{RO}PP_2$. Moreover, the final absorption spectrum of $^{RO}PP_2^{+\bullet}$, obtained after the addition of 1 equiv. of $^{RO}PP_2$ to $NAP^{+\bullet}$ solution, remained unchanged even if a large excess of (i.e. ~5 equiv) of neutral $^{RO}PP_2$ was added. Also note that decreasing of the concentration of $^{RO}PP_2^{+\bullet}$ by ten-fold did not show any changes in its absorption spectrum. Similarly, other $^{RO}PP_n^{+\bullet}$ were generated in dichloromethane, and their spectra are compiled in Figure 2C.

A comparison of the $^{RO}PP_2^{+\bullet}$–$^{RO}PP_4^{+\bullet}$ spectra showed structured absorption bands that shifted red with increasing number of *p*-phenylene units. The strikingly similar absorption spectra of $^{RO}PP_6^{+\bullet}$ and $^{RO}PP_7^{+\bullet}$ showed a Gaussian band at ~1400 nm. The spectrum of $^{RO}PP_5^{+\bullet}$ showed intermediate features with an absorption spectrum composed of two absorption bands at 1550 nm and 1980 nm.

Positions of the bands were estimated from deconvolution of the $^{RO}\mathbf{PP_{5}^{+\bullet}}$ spectrum by means of nonlinear least-square fitting, which was performed in the wavenumber units. One Gaussian-shaped band, with maximum at ~1550 nm, has full-width at half maximum (FWHM) of 1600 cm$^{-1}$, and another one, with maximum at 1980 nm, has FWHM of ~950 cm$^{-1}$. Ratio of the intensities of these two bands remains almost constant, $1.6 \pm 0.1$, with respect to incremental dilutions down to 23% of the original concentration of $^{RO}\mathbf{PP_{5}^{+\bullet}}$. At the same time, ratio of the intensities dramatically depends on temperature, as the band at 1980 nm disappears upon temperature lowering from 293 K to 233 K. These observations allowed us to suggest co-existense of two isomeric forms of $^{RO}\mathbf{PP_{5}^{+\bullet}}$, which have different hole distribution patterns. Then, band at 1980 nm can be attributed to the charge localized in the middle of the molecule (like in $^{RO}\mathbf{PP_{4}^{+\bullet}}$), and band at 1550 nm—to the charge localized at the end (like in $^{RO}\mathbf{PP_{6}^{+\bullet}}$). The case of $^{RO}\mathbf{PP_{5}^{+\bullet}}$, which represents a border-case behaviour between short and long oligomer cation radicalse, will be a subject for the forthcoming study.

## S6. Hole distribution in $^{R}PP_n^{+\bullet}$

### S6.1. Distortion of $^{R}PP_n$ geometries, caused by oxidation

Position of the hole in a given poly-*p*-phenylene molecule can be determined from the geometrical changes induced by 1-$e^-$ oxidation. In $^{iA}PP_n$, oxidation causes quinoidal distortion of *p*-phenylene units, which results in shortening of inter-ring C–C bonds and decrease of the inter-ring dihedral angle θ:
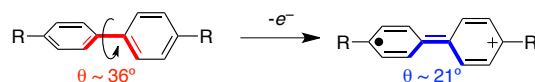


Maximum geometric distortions predicted with DFT are observed in the case of $^{R}PP_2^{+\bullet}$, where the central C–C bond length shortens from ~1.48 to ~1.43 Å, and the dihedral angle reduces from ~36° to ~21°. In longer $^{R}PP_n^{+\bullet}$, the spread of the geometric distortions depends on the chain length and the nature of the end-capping substituents, which suggests significantly different hole distribution patterns in various $^{R}PP_n^{+\bullet}$ (Figures S16–S18 and Tables S11–S13). Although the geometric distortions are useful descriptors of the hole distribution in the ground state, they cannot be used for the hole description in the vertically excited $^{R}PP_n^{+\bullet}$. At the same time, distribution patterns or position of the hole in both ground and vertically excited states of $^{R}PP_n^{+\bullet}$ can be conveniently visualized by unpaired spin density distribution plots (Figure 4 in the main text). Moreover, one can easily quantify per-unit unpaired spin $\Delta s$ (Figure S21) and positive charge $\Delta q^+$ values (Figure 4 in the main text) by natural population. There is an excellent correlation between the calculated geometric distortions and the per-unit $\Delta s$ and $\Delta q^+$ values in various $^{R}PP_n^{+\bullet}$ (Figures S22–S24).

### S6.2. Quinoidal distortion of the *p*-phenylene units
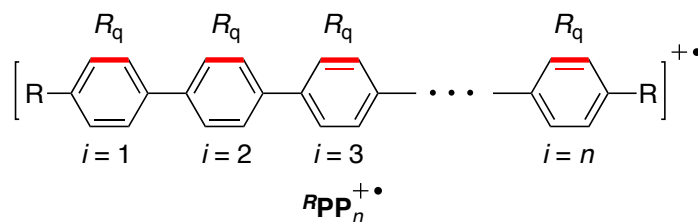
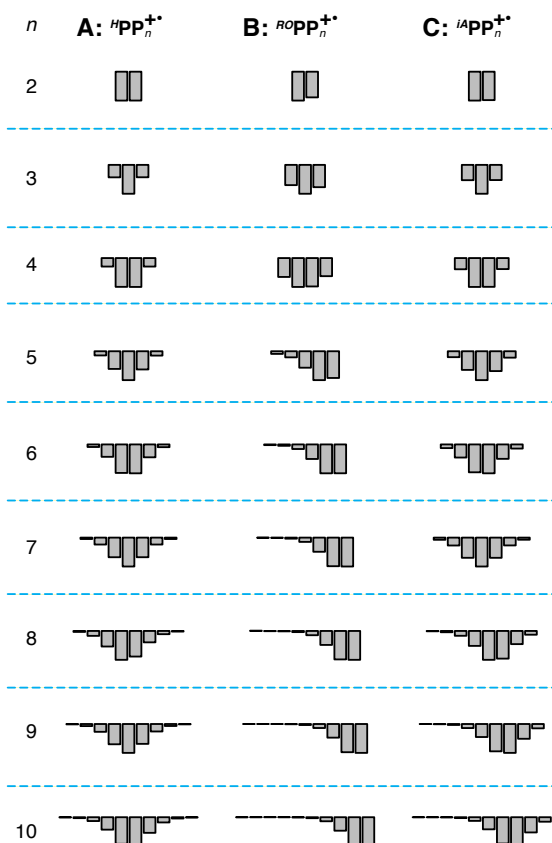**Figure S16**. Shortening of the $R_q$ distance in various $^R\text{PP}_n^{+\bullet}$ series, caused by oxidation; calculated by means of the B1LYP-40 functional.

**Table S11**. Shortening of the $R_q$ distance (in Å) in various $^R\text{PP}_n^{+\bullet}$ series, caused by oxidation; calculated by means of the B1LYP-40 functional.

| $n$ | $i$ | $^{RO}\text{PP}_n$ | | | $^{iA}\text{PP}_n$ | | | $^{H}\text{PP}_n$ | | |
|---|---|---|---|---|---|---|---|---|---|---|
| | | N | CR | Δ | N | CR | Δ | N | CR | Δ |
| 2 | 1 | 1.391 | 1.370 | 0.021 | 1.389 | 1.371 | 0.018 | 1.389 | 1.372 | 0.017 |
| 2 | 2 | 1.382 | 1.363 | 0.019 | 1.387 | 1.369 | 0.018 | 1.389 | 1.372 | 0.017 |
| 3 | 1 | 1.382 | 1.369 | 0.013 | 1.389 | 1.378 | 0.011 | 1.389 | 1.379 | 0.009 |
| 3 | 2 | 1.386 | 1.367 | 0.019 | 1.386 | 1.365 | 0.021 | 1.386 | 1.365 | 0.021 |
| 3 | 3 | 1.391 | 1.376 | 0.015 | 1.386 | 1.376 | 0.011 | 1.389 | 1.379 | 0.009 |
| 4 | 1 | 1.391 | 1.380 | 0.010 | 1.386 | 1.380 | 0.006 | 1.389 | 1.384 | 0.005 |
| 4 | 2 | 1.386 | 1.370 | 0.016 | 1.386 | 1.369 | 0.017 | 1.386 | 1.369 | 0.017 |
| 4 | 3 | 1.386 | 1.370 | 0.015 | 1.386 | 1.369 | 0.017 | 1.386 | 1.369 | 0.017 |
| 4 | 4 | 1.391 | 1.381 | 0.010 | 1.386 | 1.380 | 0.006 | 1.389 | 1.384 | 0.005 |
| 5 | 1 | 1.391 | 1.389 | 0.002 | 1.389 | 1.385 | 0.004 | 1.389 | 1.386 | 0.003 |
| 5 | 2 | 1.386 | 1.382 | 0.004 | 1.386 | 1.375 | 0.011 | 1.386 | 1.375 | 0.011 |
| 5 | 3 | 1.386 | 1.376 | 0.010 | 1.386 | 1.368 | 0.017 | 1.386 | 1.367 | 0.018 |
| 5 | 4 | 1.386 | 1.368 | 0.018 | 1.386 | 1.374 | 0.012 | 1.386 | 1.374 | 0.012 |
| 5 | 5 | 1.391 | 1.374 | 0.016 | 1.389 | 1.385 | 0.004 | 1.389 | 1.386 | 0.003 |

| $n$ | $i$ | $^{RO}\text{PP}_n$ | | | $^{iA}\text{PP}_n$ | | | $^{H}\text{PP}_n$ | | |
|---|---|---|---|---|---|---|---|---|---|---|
| | | N | CR | Δ | N | CR | Δ | N | CR | Δ |
| 6 | 1 | 1.391 | 1.390 | 0.000 | 1.389 | 1.387 | 0.002 | 1.389 | 1.387 | 0.001 |
| 6 | 2 | 1.386 | 1.385 | 0.001 | 1.386 | 1.379 | 0.007 | 1.386 | 1.379 | 0.007 |
| 6 | 3 | 1.386 | 1.383 | 0.003 | 1.386 | 1.371 | 0.015 | 1.386 | 1.370 | 0.016 |
| 6 | 4 | 1.386 | 1.377 | 0.009 | 1.386 | 1.370 | 0.015 | 1.386 | 1.370 | 0.016 |
| 6 | 5 | 1.386 | 1.368 | 0.018 | 1.386 | 1.378 | 0.008 | 1.386 | 1.379 | 0.007 |
| 6 | 6 | 1.391 | 1.373 | 0.018 | 1.386 | 1.384 | 0.002 | 1.389 | 1.387 | 0.001 |
| 7 | 1 | 1.382 | 1.382 | 0.000 | 1.389 | 1.387 | 0.001 | 1.389 | 1.388 | 0.001 |
| 7 | 2 | 1.386 | 1.386 | 0.000 | 1.386 | 1.381 | 0.004 | 1.386 | 1.382 | 0.004 |
| 7 | 3 | 1.386 | 1.385 | 0.001 | 1.386 | 1.374 | 0.011 | 1.386 | 1.374 | 0.011 |
| 7 | 4 | 1.386 | 1.383 | 0.003 | 1.386 | 1.370 | 0.016 | 1.386 | 1.369 | 0.017 |
| 7 | 5 | 1.386 | 1.377 | 0.009 | 1.386 | 1.374 | 0.011 | 1.386 | 1.374 | 0.011 |
| 7 | 6 | 1.386 | 1.368 | 0.018 | 1.386 | 1.382 | 0.004 | 1.386 | 1.382 | 0.004 |
| 7 | 7 | 1.391 | 1.373 | 0.018 | 1.386 | 1.385 | 0.001 | 1.389 | 1.388 | 0.001 |
| 8 | 1 | 1.382 | 1.382 | 0.000 | 1.389 | 1.388 | 0.000 | 1.389 | 1.388 | 0.001 |
| 8 | 2 | 1.386 | 1.386 | 0.000 | 1.386 | 1.385 | 0.001 | 1.386 | 1.383 | 0.003 |
| 8 | 3 | 1.386 | 1.386 | 0.000 | 1.386 | 1.383 | 0.003 | 1.386 | 1.377 | 0.008 |
| 8 | 4 | 1.386 | 1.385 | 0.001 | 1.386 | 1.378 | 0.008 | 1.386 | 1.370 | 0.016 |
| 8 | 5 | 1.386 | 1.383 | 0.003 | 1.386 | 1.371 | 0.015 | 1.386 | 1.372 | 0.014 |
| 8 | 6 | 1.386 | 1.377 | 0.009 | 1.386 | 1.371 | 0.014 | 1.386 | 1.380 | 0.006 |
| 8 | 7 | 1.386 | 1.368 | 0.018 | 1.386 | 1.379 | 0.007 | 1.386 | 1.384 | 0.002 |
| 8 | 8 | 1.391 | 1.373 | 0.018 | 1.386 | 1.384 | 0.002 | 1.389 | 1.388 | 0.000 |
| 9 | 1 | 1.382 | 1.382 | 0.000 | 1.389 | 1.389 | 0.000 | 1.389 | 1.388 | 0.000 |
| 9 | 2 | 1.386 | 1.386 | 0.000 | 1.386 | 1.386 | 0.000 | 1.386 | 1.385 | 0.001 |
| 9 | 3 | 1.386 | 1.386 | 0.000 | 1.386 | 1.385 | 0.001 | 1.386 | 1.381 | 0.004 |
| 9 | 4 | 1.386 | 1.386 | 0.000 | 1.386 | 1.384 | 0.002 | 1.386 | 1.374 | 0.011 |
| 9 | 5 | 1.386 | 1.385 | 0.001 | 1.386 | 1.379 | 0.007 | 1.386 | 1.370 | 0.016 |
| 9 | 6 | 1.386 | 1.383 | 0.002 | 1.386 | 1.371 | 0.015 | 1.386 | 1.375 | 0.011 |
| 9 | 7 | 1.386 | 1.377 | 0.008 | 1.386 | 1.370 | 0.015 | 1.386 | 1.382 | 0.004 |
| 9 | 8 | 1.386 | 1.368 | 0.018 | 1.386 | 1.378 | 0.008 | 1.386 | 1.385 | 0.001 |
| 9 | 9 | 1.391 | 1.373 | 0.018 | 1.386 | 1.384 | 0.002 | 1.389 | 1.388 | 0.000 |
| 10 | 1 | 1.382 | 1.382 | 0.000 | 1.389 | 1.389 | 0.000 | 1.389 | 1.388 | 0.000 |
| 10 | 2 | 1.386 | 1.386 | 0.000 | 1.386 | 1.386 | 0.000 | 1.386 | 1.385 | 0.000 |
| 10 | 3 | 1.386 | 1.386 | 0.000 | 1.386 | 1.386 | 0.000 | 1.386 | 1.384 | 0.002 |
| 10 | 4 | 1.386 | 1.386 | 0.000 | 1.386 | 1.385 | 0.000 | 1.386 | 1.379 | 0.007 |
| 10 | 5 | 1.386 | 1.386 | 0.000 | 1.386 | 1.384 | 0.002 | 1.386 | 1.372 | 0.014 |
| 10 | 6 | 1.386 | 1.385 | 0.001 | 1.386 | 1.379 | 0.007 | 1.386 | 1.371 | 0.015 |
| 10 | 7 | 1.386 | 1.383 | 0.003 | 1.386 | 1.372 | 0.014 | 1.386 | 1.378 | 0.008 |
| 10 | 8 | 1.386 | 1.377 | 0.009 | 1.386 | 1.370 | 0.016 | 1.386 | 1.383 | 0.003 |
| 10 | 9 | 1.386 | 1.368 | 0.018 | 1.386 | 1.378 | 0.008 | 1.386 | 1.385 | 0.001 |
| 10 | 10 | 1.391 | 1.372 | 0.018 | 1.386 | 1.384 | 0.002 | 1.389 | 1.388 | 0.000 |

## 6.2.1  Shortening of the distance between *p*-phenylene units



**Figure S17**. Shortening of the $R_C$ distance in various $^R\text{PP}_n$ series, caused by oxidation; calculated by means of the B1LYP-40 functional. Note that each bar plot contains $n-1$ bars, as there are $n-1$ bonds between *p*-phenylene units in $^R\text{PP}_n^{+\bullet}$.
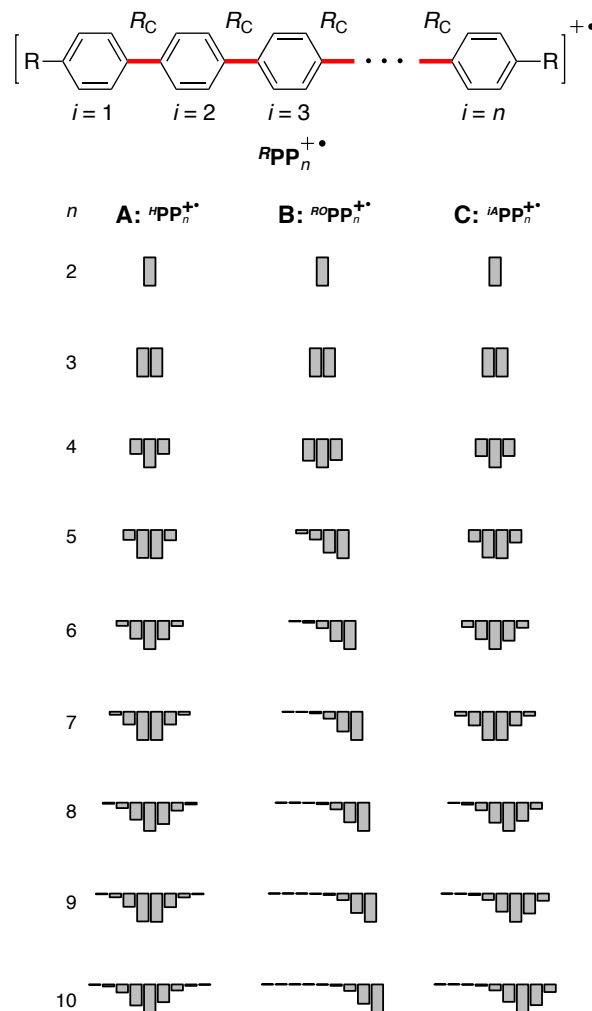
**Table S12**. Shortening of the $R_C$ distance (in Å) in various $^R\text{PP}_n^{+\bullet}$ series, caused by oxidation; calculated by means of the B1LYP-40 functional.

| $n$ | $i–j$ | $^{RO}\text{PP}_n$ | | | $^{iA}\text{PP}_n$ | | | $^{H}\text{PP}_n$ | | |
|---|---|---|---|---|---|---|---|---|---|---|
| | | N | CR | Δ | N | CR | Δ | N | CR | Δ |
| 2 | 1-2 | 1.481 | 1.434 | 0.047 | 1.482 | 1.433 | 0.048 | 1.483 | 1.434 | 0.050 |
| 3 | 1-2 | 1.480 | 1.443 | 0.037 | 1.481 | 1.444 | 0.037 | 1.482 | 1.446 | 0.036 |
| 3 | 2-3 | 1.480 | 1.443 | 0.037 | 1.481 | 1.444 | 0.037 | 1.482 | 1.446 | 0.036 |
| 4 | 1-2 | 1.480 | 1.453 | 0.027 | 1.481 | 1.457 | 0.024 | 1.482 | 1.460 | 0.022 |
| 4 | 2-3 | 1.480 | 1.444 | 0.036 | 1.480 | 1.441 | 0.040 | 1.480 | 1.439 | 0.041 |
| 4 | 3-4 | 1.480 | 1.454 | 0.026 | 1.481 | 1.457 | 0.024 | 1.482 | 1.460 | 0.022 |

| $n$ | $i$–$j$ | $^{RO}PP_n$ | | | $^{iA}PP_n$ | | | $^{H}PP_n$ | | |
|---|---|---|---|---|---|---|---|---|---|---|
| | | N | CR | Δ | N | CR | Δ | N | CR | Δ |
| 5 | 1-2 | 1.480 | 1.476 | 0.004 | 1.481 | 1.467 | 0.014 | 1.482 | 1.470 | 0.012 |
| 5 | 2-3 | 1.480 | 1.467 | 0.013 | 1.480 | 1.447 | 0.033 | 1.480 | 1.446 | 0.034 |
| 5 | 3-4 | 1.480 | 1.450 | 0.030 | 1.480 | 1.447 | 0.034 | 1.480 | 1.446 | 0.034 |
| 5 | 4-5 | 1.480 | 1.442 | 0.038 | 1.481 | 1.466 | 0.015 | 1.482 | 1.469 | 0.012 |
| 6 | 1-2 | 1.480 | 1.479 | 0.001 | 1.481 | 1.473 | 0.008 | 1.482 | 1.475 | 0.006 |
| 6 | 2-3 | 1.480 | 1.477 | 0.003 | 1.480 | 1.457 | 0.023 | 1.480 | 1.457 | 0.023 |
| 6 | 3-4 | 1.480 | 1.470 | 0.010 | 1.480 | 1.445 | 0.035 | 1.480 | 1.443 | 0.037 |
| 6 | 4-5 | 1.480 | 1.452 | 0.028 | 1.480 | 1.455 | 0.025 | 1.480 | 1.456 | 0.024 |
| 6 | 5-6 | 1.480 | 1.440 | 0.040 | 1.481 | 1.472 | 0.009 | 1.482 | 1.475 | 0.007 |
| 7 | 1-2 | 1.480 | 1.440 | 0.040 | 1.481 | 1.477 | 0.004 | 1.482 | 1.478 | 0.003 |
| 7 | 2-3 | 1.480 | 1.452 | 0.028 | 1.480 | 1.465 | 0.015 | 1.480 | 1.466 | 0.015 |
| 7 | 3-4 | 1.480 | 1.470 | 0.010 | 1.480 | 1.449 | 0.031 | 1.480 | 1.448 | 0.032 |
| 7 | 4-5 | 1.480 | 1.478 | 0.002 | 1.480 | 1.449 | 0.031 | 1.480 | 1.448 | 0.032 |
| 7 | 5-6 | 1.480 | 1.480 | 0.000 | 1.480 | 1.465 | 0.015 | 1.480 | 1.466 | 0.015 |
| 7 | 6-7 | 1.480 | 1.480 | 0.000 | 1.481 | 1.477 | 0.004 | 1.482 | 1.478 | 0.003 |
| 8 | 1-2 | 1.480 | 1.440 | 0.040 | 1.481 | 1.473 | 0.008 | 1.482 | 1.480 | 0.001 |
| 8 | 2-3 | 1.480 | 1.452 | 0.028 | 1.480 | 1.458 | 0.022 | 1.480 | 1.474 | 0.007 |
| 8 | 3-4 | 1.480 | 1.471 | 0.010 | 1.480 | 1.445 | 0.035 | 1.480 | 1.459 | 0.021 |
| 8 | 4-5 | 1.480 | 1.478 | 0.002 | 1.480 | 1.456 | 0.025 | 1.480 | 1.446 | 0.035 |
| 8 | 5-6 | 1.480 | 1.480 | 0.000 | 1.480 | 1.471 | 0.009 | 1.480 | 1.454 | 0.026 |
| 8 | 6-7 | 1.480 | 1.480 | 0.000 | 1.480 | 1.478 | 0.002 | 1.480 | 1.471 | 0.010 |
| 8 | 7-8 | 1.480 | 1.480 | 0.000 | 1.481 | 1.480 | 0.001 | 1.482 | 1.480 | 0.002 |
| 9 | 1-2 | 1.480 | 1.440 | 0.040 | 1.481 | 1.472 | 0.009 | 1.482 | 1.481 | 0.001 |
| 9 | 2-3 | 1.480 | 1.452 | 0.028 | 1.480 | 1.456 | 0.025 | 1.480 | 1.476 | 0.004 |
| 9 | 3-4 | 1.480 | 1.471 | 0.009 | 1.480 | 1.445 | 0.035 | 1.480 | 1.465 | 0.015 |
| 9 | 4-5 | 1.480 | 1.478 | 0.002 | 1.480 | 1.458 | 0.022 | 1.480 | 1.449 | 0.031 |
| 9 | 5-6 | 1.480 | 1.480 | 0.000 | 1.480 | 1.472 | 0.008 | 1.480 | 1.449 | 0.031 |
| 9 | 6-7 | 1.480 | 1.480 | 0.000 | 1.480 | 1.478 | 0.002 | 1.480 | 1.465 | 0.015 |
| 9 | 7-8 | 1.480 | 1.480 | 0.000 | 1.480 | 1.480 | 0.000 | 1.480 | 1.476 | 0.004 |
| 9 | 8-9 | 1.480 | 1.480 | 0.000 | 1.481 | 1.481 | 0.000 | 1.482 | 1.481 | 0.001 |
| 10 | 1-2 | 1.480 | 1.440 | 0.040 | 1.481 | 1.472 | 0.009 | 1.482 | 1.481 | 0.000 |
| 10 | 2-3 | 1.480 | 1.453 | 0.028 | 1.480 | 1.455 | 0.026 | 1.480 | 1.478 | 0.002 |
| 10 | 3-4 | 1.480 | 1.471 | 0.009 | 1.480 | 1.445 | 0.035 | 1.480 | 1.470 | 0.010 |
| 10 | 4-5 | 1.480 | 1.478 | 0.002 | 1.480 | 1.459 | 0.022 | 1.480 | 1.455 | 0.025 |
| 10 | 5-6 | 1.480 | 1.480 | 0.000 | 1.480 | 1.473 | 0.007 | 1.480 | 1.446 | 0.034 |
| 10 | 6-7 | 1.480 | 1.480 | 0.000 | 1.480 | 1.479 | 0.002 | 1.480 | 1.459 | 0.021 |
| 10 | 7-8 | 1.480 | 1.480 | 0.000 | 1.480 | 1.480 | 0.000 | 1.480 | 1.473 | 0.007 |
| 10 | 8-9 | 1.480 | 1.480 | 0.000 | 1.480 | 1.480 | 0.000 | 1.480 | 1.479 | 0.002 |
| 10 | 9-10 | 1.480 | 1.480 | 0.000 | 1.481 | 1.481 | 0.000 | 1.482 | 1.482 | 0.000 |

## 6.2.2 Planarization of substituted oligo-*p*-phenylene units
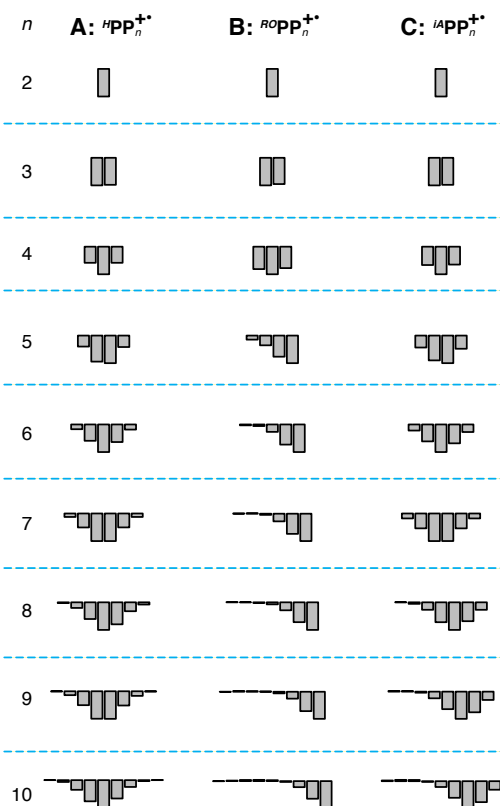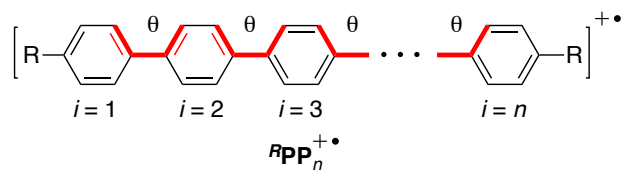




**Figure S18**. Decrease in the central dihedral angle $\theta$ in $^R$PP$_n$, caused by oxidation; calculated by means of the B1LYP-40 functional. Note that each barplot contains $n-1$ bars, as there are $n-1$ bonds between *p*-phenylene units in $^R$PP$_n^{+\cdot}$.

**Table S13**. Decrease in the central dihedral angle $\theta$ in $^R$PP$_n$, caused by oxidation; calculated by means of the B1LYP-40 functional

| $n$ | $i\text{-}j$ | $^{RO}$PP$_n$ | | | $^{iA}$PP$_n$ | | | $^H$PP$_n$ | | |
|-----|------|------|------|------|------|------|------|------|------|------|
| | | N | CR | $\Delta$ | N | CR | $\Delta$ | N | CR | $\Delta$ |
| 2 | 1-2 | 36.7 | -15.1 | 21.6 | 36.8 | 15.0 | 21.8 | 38.0 | 16.3 | 21.7 |
| 3 | 1-2 | 35.8 | -18.1 | 17.7 | 36.1 | 19.2 | 16.9 | 36.8 | -20.2 | 16.5 |
| 3 | 2-3 | -35.8 | -18.9 | 16.9 | -36.1 | 19.6 | 16.5 | -36.8 | -20.6 | 16.2 |
| 4 | 1-2 | -35.8 | -22.7 | 13.1 | -36.1 | -24.6 | 11.5 | -36.8 | -26.2 | 10.6 |
| 4 | 2-3 | 35.5 | -19.4 | 16.1 | 35.6 | -18.3 | 17.3 | 35.8 | -17.7 | 18.1 |
| 4 | 3-4 | -35.9 | -23.3 | 12.5 | -36.1 | -24.9 | 11.2 | -36.8 | -26.2 | 10.6 |

| $n$ | $i$-$j$ | $^{RO}\mathbf{PP}_n$ | | | $^{iA}\mathbf{PP}_n$ | | | $^{H}\mathbf{PP}_n$ | | |
|---|---|---|---|---|---|---|---|---|---|---|
| | | N | CR | Δ | N | CR | Δ | N | CR | Δ |
| 5 | 1-2 | -35.9 | -33.3 | 2.6 | -36.2 | -29.2 | 7.0 | 36.9 | -30.7 | 6.1 |
| 5 | 2-3 | -35.6 | -29.4 | 6.2 | 35.7 | -21.2 | 14.5 | -35.7 | -21.2 | 14.5 |
| 5 | 3-4 | -35.6 | -22.1 | 13.4 | -35.7 | -19.6 | 16.1 | 35.7 | -20.3 | 15.4 |
| 5 | 4-5 | 35.9 | -18.3 | 17.5 | 36.2 | -28.5 | 7.7 | -36.9 | -30.5 | 6.4 |
| 6 | 1-2 | -35.8 | -35.2 | 0.6 | -36.2 | -32.3 | 3.8 | -36.8 | -33.7 | 3.1 |
| 6 | 2-3 | 35.6 | -34.5 | 1.0 | 35.7 | -25.1 | 10.7 | 35.7 | -25.1 | 10.6 |
| 6 | 3-4 | -35.7 | -30.8 | 4.9 | -35.7 | -18.3 | 17.4 | -35.7 | -17.7 | 17.9 |
| 6 | 4-5 | 35.5 | -22.3 | 13.2 | 35.7 | -23.8 | 11.9 | 35.7 | -24.3 | 11.4 |
| 6 | 5-6 | -35.8 | -17.8 | 18.1 | -36.2 | -31.4 | 4.8 | -36.8 | -33.5 | 3.3 |
| 7 | 1-2 | -35.8 | -17.7 | 18.1 | -36.2 | -33.7 | 2.5 | -36.8 | -35.0 | 1.8 |
| 7 | 2-3 | -35.5 | -22.1 | 13.4 | 35.7 | -28.1 | 7.6 | 35.7 | -28.5 | 7.2 |
| 7 | 3-4 | -35.6 | -30.6 | 5.1 | -35.7 | -21.6 | 14.1 | -35.6 | -21.4 | 14.2 |
| 7 | 4-5 | 35.6 | -34.8 | 0.8 | 35.7 | -21.6 | 14.1 | 35.6 | -21.4 | 14.2 |
| 7 | 5-6 | -35.6 | -35.9 | -0.3 | -35.7 | -28.1 | 7.6 | -35.7 | -28.5 | 7.2 |
| 7 | 6-7 | 35.7 | -35.9 | -0.2 | 36.2 | -33.6 | 2.5 | 36.8 | -35.0 | 1.8 |
| 8 | 1-2 | -36.0 | -17.7 | 18.3 | -36.2 | -32.0 | 4.2 | -36.8 | -36.4 | 0.5 |
| 8 | 2-3 | 35.5 | -22.4 | 13.1 | 35.7 | -25.2 | 10.5 | 35.7 | -32.5 | 3.2 |
| 8 | 3-4 | -35.7 | -30.5 | 5.3 | -35.6 | -20.3 | 15.4 | -35.7 | -26.0 | 9.6 |
| 8 | 4-5 | 35.6 | -34.3 | 1.3 | 35.7 | -24.6 | 11.1 | 35.7 | -19.8 | 15.9 |
| 8 | 5-6 | -35.7 | -35.3 | 0.4 | -35.7 | -31.5 | 4.2 | -35.7 | -23.0 | 12.7 |
| 8 | 6-7 | 35.6 | -35.6 | 0.0 | 35.7 | -34.9 | 0.8 | 35.8 | -30.6 | 5.1 |
| 8 | 7-8 | -35.8 | -35.9 | -0.1 | -36.2 | -36.2 | -0.1 | -36.8 | -35.5 | 1.3 |
| 9 | 1-2 | -35.9 | -17.9 | 18.1 | -36.1 | -31.3 | 4.8 | -36.8 | -36.7 | 0.1 |
| 9 | 2-3 | 35.6 | -22.7 | 12.9 | 35.7 | -23.7 | 12.0 | 35.8 | -33.7 | 2.1 |
| 9 | 3-4 | -35.7 | -31.1 | 4.6 | -35.6 | -19.8 | 15.8 | -35.7 | -28.3 | 7.4 |
| 9 | 4-5 | 35.7 | -34.6 | 1.1 | 35.7 | -25.5 | 10.2 | 35.7 | -21.1 | 14.6 |
| 9 | 5-6 | -35.7 | -35.9 | -0.2 | -35.7 | -31.8 | 3.9 | -35.7 | -21.0 | 14.7 |
| 9 | 6-7 | 35.7 | -36.1 | -0.4 | 35.7 | -35.0 | 0.6 | 35.7 | -28.1 | 7.6 |
| 9 | 7-8 | -35.6 | -36.1 | -0.5 | -35.8 | -36.1 | -0.4 | -35.8 | -33.3 | 2.5 |
| 9 | 8-9 | 35.9 | -35.8 | 0.0 | 36.1 | -36.5 | -0.4 | 36.8 | -36.6 | 0.2 |
| 10 | 1-2 | -36.0 | -16.4 | 19.6 | -36.1 | -31.1 | 5.0 | -36.9 | -36.9 | 0.0 |
| 10 | 2-3 | 35.5 | -22.5 | 13.0 | 35.7 | -23.4 | 12.3 | 35.7 | -34.7 | 1.0 |
| 10 | 3-4 | -35.8 | -31.3 | 4.5 | -35.6 | -20.0 | 15.6 | -35.7 | -30.4 | 5.3 |
| 10 | 4-5 | 35.6 | -35.0 | 0.6 | 35.7 | -25.9 | 9.8 | 35.6 | -24.0 | 11.6 |
| 10 | 5-6 | -35.7 | -36.4 | -0.7 | -35.6 | -32.2 | 3.4 | -35.7 | -20.5 | 15.2 |
| 10 | 6-7 | 35.6 | -36.5 | -0.9 | 35.7 | -35.3 | 0.4 | 35.7 | -25.6 | 10.1 |
| 10 | 7-8 | -35.6 | -36.5 | -0.8 | -35.6 | -36.3 | -0.7 | -35.7 | -31.9 | 3.7 |
| 10 | 8-9 | 35.6 | -36.0 | -0.4 | 35.7 | -36.5 | -0.8 | 35.7 | -35.2 | 0.5 |
| 10 | 9-10 | -35.8 | -35.7 | 0.1 | -36.2 | -36.6 | -0.4 | -36.8 | -36.9 | -0.1 |

## S6.3. Highest occupied molecular orbitals of $^{R}PP_n$
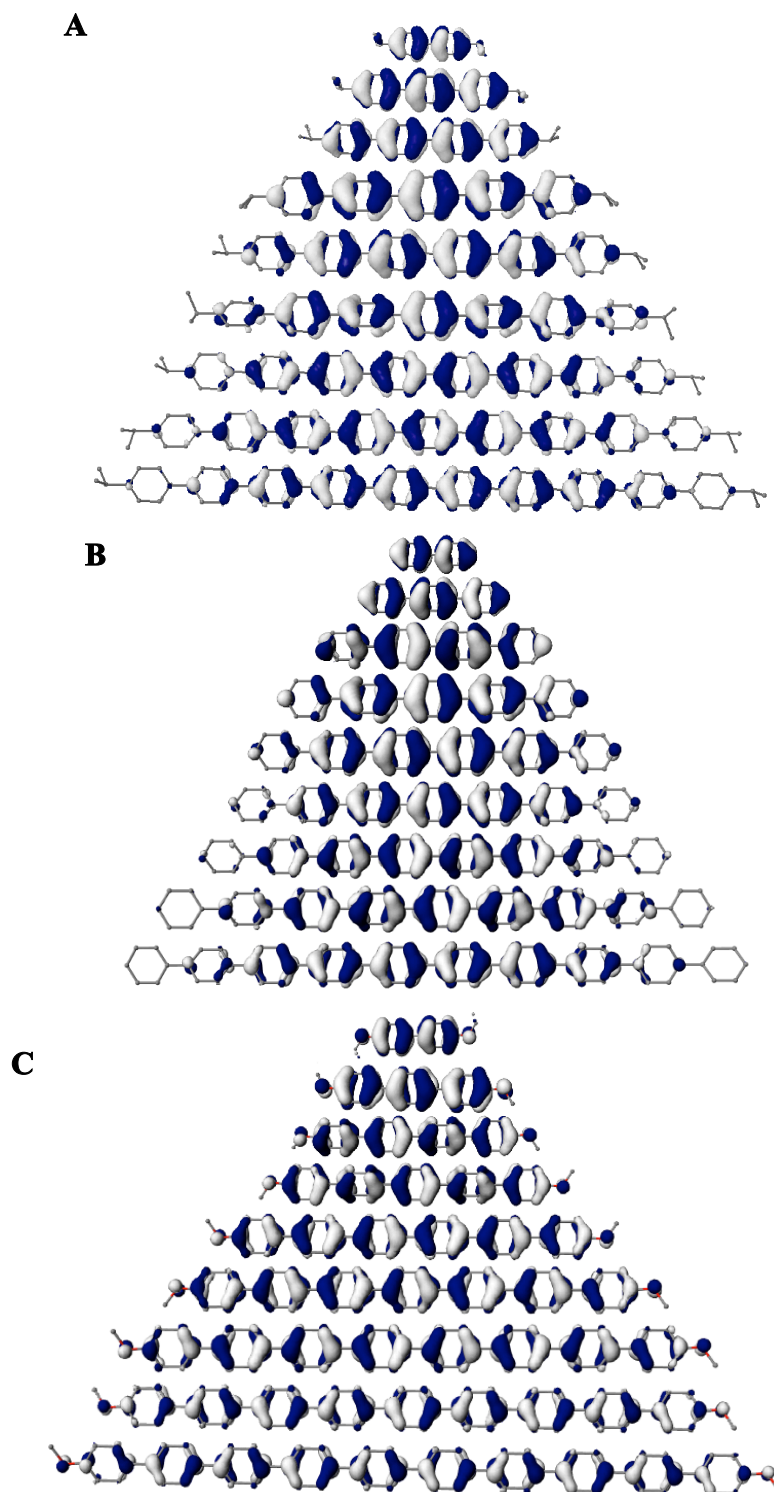


**Figure S19**. Isovalue plots (0.03 a.u.) of the highest occupied molecular orbitals of $^{iA}PP_n$ (A), $^{H}PP_n$ (B), and $^{RO}PP_n$ (C) calculated by means of B1LYP-40. HOMOs are always centered in the middle of the chain and much more delocalized comparing to the corresponding hole distributions.

**S6.4. Spatial distribution of the difference between electron density distribution in the neutral and cation radical forms of $^{iA}PP_n$**
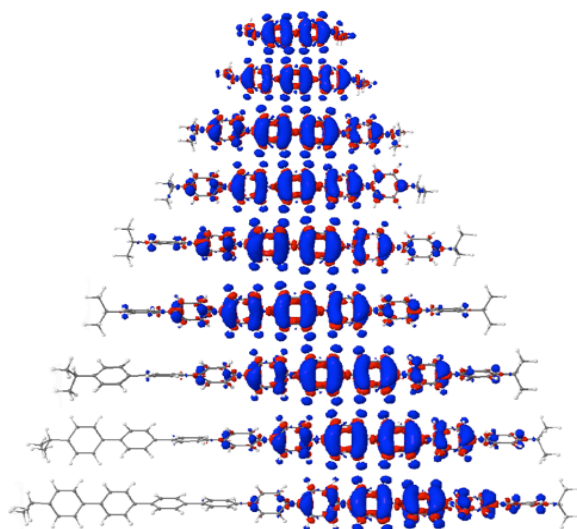


**Figure S20**. Difference between the spatial electron density distributions in the $^{iA}PP_n$ and $^{iA}PP_n^{+\bullet}$, with the geometries corresponding to $^{iA}PP_n^{+\bullet}$. Calculations were performed by means of the B1LYP-40 functional.

## S6.5. Per-unit spin distribution in $^R\text{PP}_n^{+\bullet}$

The per-unit distributions of unpaired spin density in $^R\text{PP}_n^{+\bullet}$ (Figure S21), obtained using the natural population analysis (NPA), provide generally the same picture as the per-unit NPA charge distributions (Figure 4 in the main text). Subtle differences between these plots are most present on the terminal units (see also Figures S22–S24 of the next section). This deviation between spin and charge density distributions originates from the spin polarization inside $p$-phenylene units, in which some atoms might have excess of the α-electron (spin-up) density, and the others—excess of the β-electron (spin-down) density; the per-unit summation of the unpaired spin density leads to (partial) cancellation of these terms. This effect can be seen best in the excited $^{RO}\text{PP}_n^{+\bullet}$, $n \geq 5$: while the most occupied terminal unit appears to be not involved in the vertically excited state, Figure 4 in the main text clearly demonstrates significant occupation and spin-polarization of that unit.
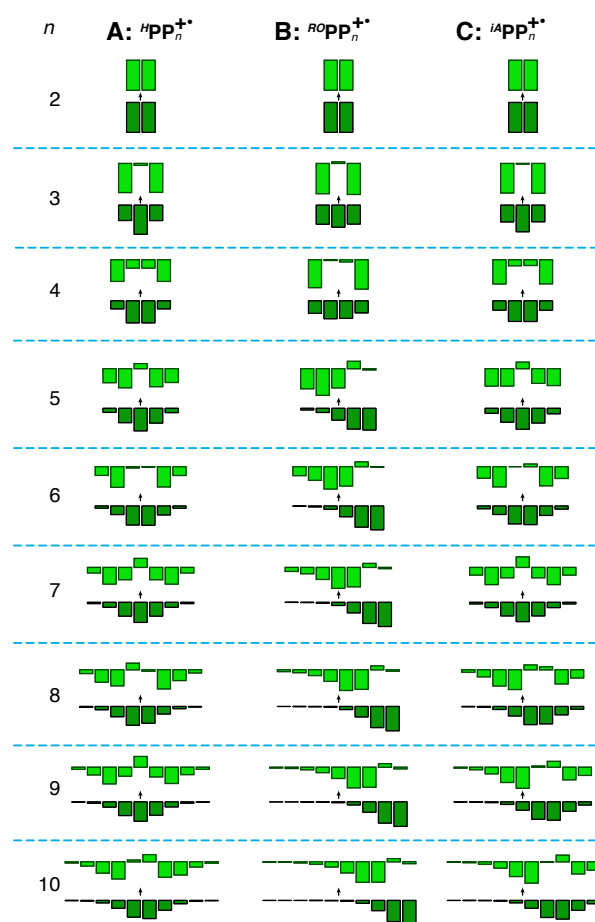


**Figure S21**. Bar charts displaying condensed per-unit unpaired spin densities in the ground- and excited state $^R\text{PP}_n^{+\bullet}$, calculated using B1LYP-40 functional.

### S6.6. Correlations between different metrics of estimation of hole position/delocalization

The distribution of the hole in various $^{R}\mathbf{PP}_n^{+\bullet}$ series can be established either through the analysis of geometrical distortions with respect to removal of electron, or directly through the analysis of the electron density in the corresponding cation radicals. We used $\Delta R_q$ parameter as a structural metrics, and employed natural population analysis (NPA) charges ($q_\alpha$ + $q_\beta$) and spins ($q_\alpha - q_\beta$), summed over each of the monomer units, to analyze the electron density of the $^{R}\mathbf{PP}_n^{+\bullet}$. Figures S22–S24 show that these different approaches predict very similar hole distribution patterns for all three $^{R}\mathbf{PP}_n^{+\bullet}$ series, although internal and external units expectedly demonstrate slightly different trends. Therefore, any of the considered metrics can be used for analysis of hole position/delocalization in $^{R}\mathbf{PP}_n^{+\bullet}$; in the manuscript, we will use spin/charge density distribution in $^{R}\mathbf{PP}_n^{+\bullet}$ due to its convenience for visualization purposes and availability for evaluation of the hole distribution in the excited state.
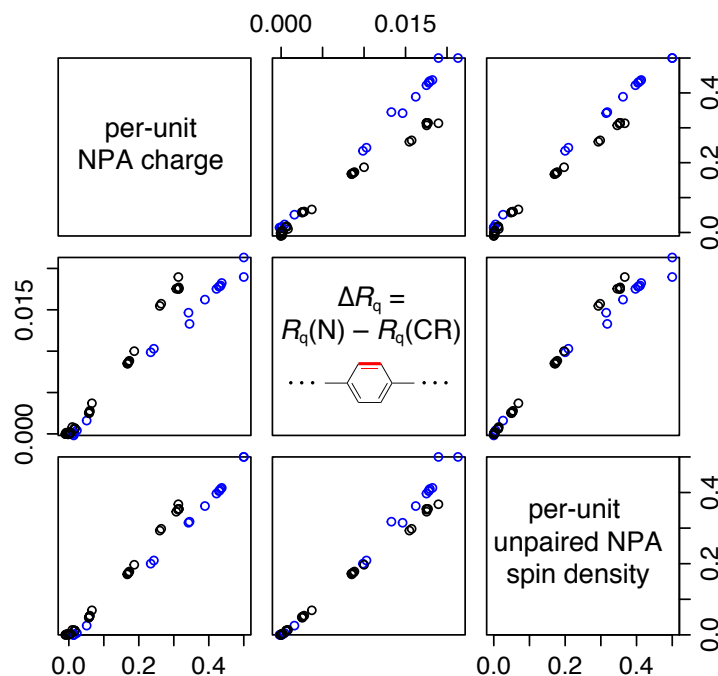


**Figure S22**. Comparison of three different approaches to estimate distribution of the hole in $^{RO}\mathbf{PP}_n^{+\bullet}$. Black points correspond to the internal units, and blue points–to the terminal alkoxy-capped units. Calculations were performed by means of the B1LYP-40 functional.
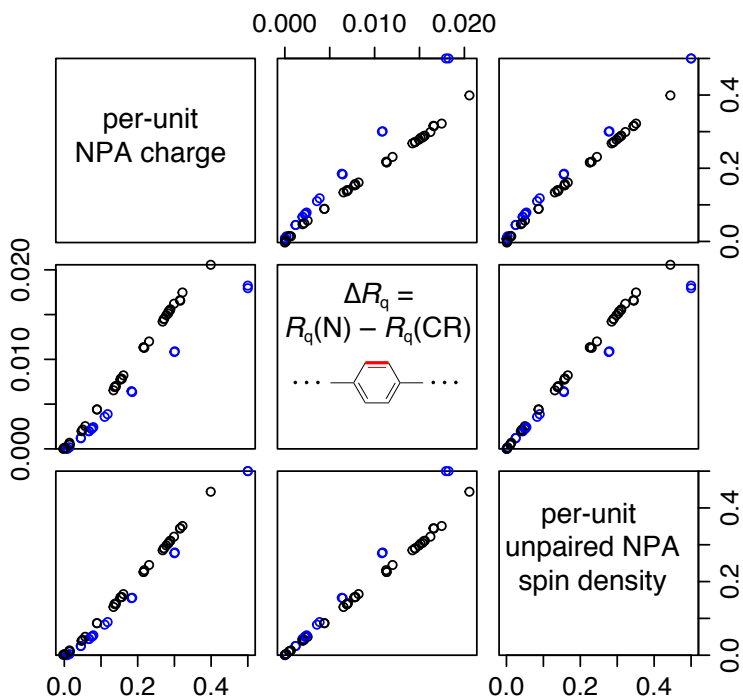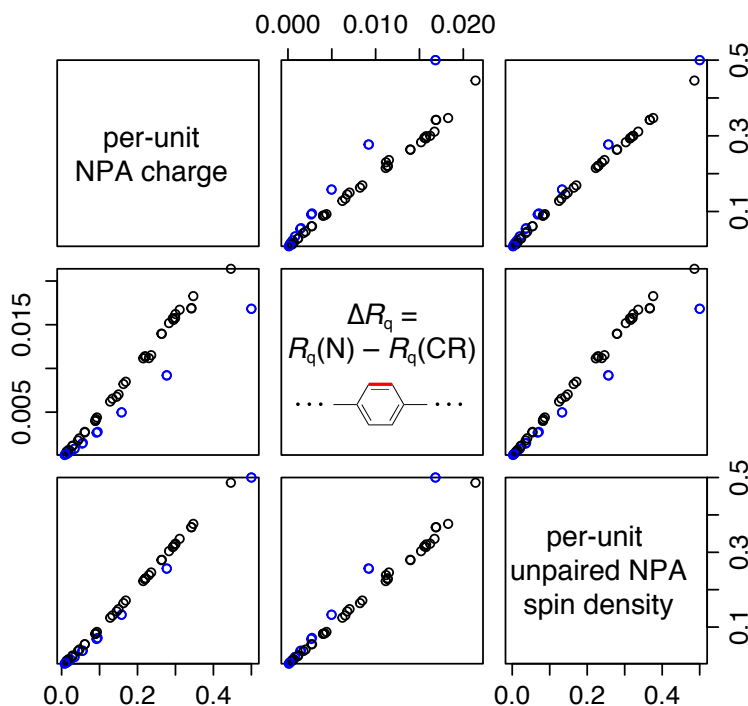
**Figure S23**. Comparison of three different approaches to estimate distribution of the hole over $^{iA}\mathbf{PP}_n^{+\bullet}$. Black points correspond to the internal units, and blue points–to the terminal alkoxy-capped units. Calculations were performed by means of the B1LYP-40 functional.



**Figure S24**. Comparison of three different approaches to estimate distribution of the hole over $^{iA}\mathbf{PP}_n^{+\bullet}$. Black points correspond to the internal units, and blue points–to the terminal alkoxy-capped units. Calculations were performed by means of the B1LYP-40 functional.

## S7. Two-parabola model of charge transfer

To develop a general multi-state parabolic model of $^R\mathbf{PP}_n^{+\bullet}$, we start with the lowest oligomers $^R\mathbf{PP}_2^{+\bullet}$ with only two redox-active units. In this case, a clear quantitative understanding can be obtained by considering interaction between two diabatic states represented by parabolic functions of the effective geometric/solvent coordinate $x$.[24] Each diabatic state corresponds to the hole exclusively localized on the respective single unit. Mathematically, the (free) energies of each diabatic states are then represented by two quadratic functions, one with the minimum at $x = 0$, and the other with the minimum at $x = 1$:

$$G_a = \lambda x^2; G_b = \lambda(1 - x)^2, \qquad \text{(Eq. S2)}$$

where $\lambda$ is the reorganization energy, which corresponds to the vertical energy gap between the two diabatic states either at $x = 0$ or 1 (Figure S25). The two adiabatic states $\Psi_1$ and $\Psi_2$ arise from the two diabatic states $\psi_a$ and $\psi_b$ mixed as:

$$\Psi_1 = c_{11}\psi_a + c_{21}\psi_b,$$
$$\Psi_2 = c_{12}\psi_a + c_{22}\psi_b. \qquad \text{(Eq. S3a)}$$

or, in matrix notation:

$$\psi_a = \begin{bmatrix} 1 \\ 0 \end{bmatrix}, \psi_b = \begin{bmatrix} 0 \\ 1 \end{bmatrix}, \quad \mathbf{\Psi} = \begin{matrix} \Psi_1 & \Psi_2 \\ \begin{bmatrix} c_{11} & c_{12} \\ c_{21} & c_{22} \end{bmatrix} \end{matrix}. \qquad \text{(Eq. S3b)}$$
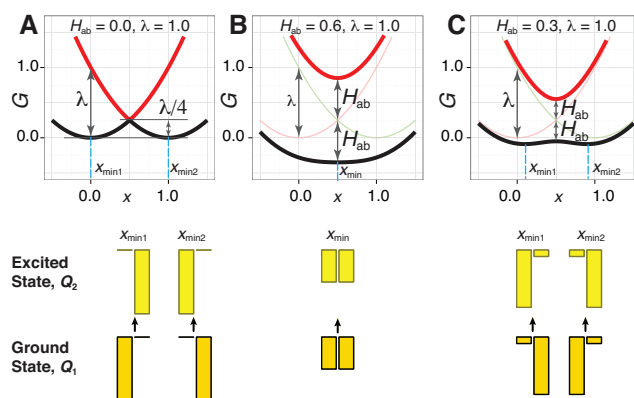


**Figure S25** (The same as Figure 6 in the main text). Free energy curves of the diabatic (thin lines) and adiabatic (thick lines) states in the three regimes of the two-parabolic model: no interaction between diabatic states, $|H_{ab}|/\lambda \approx 0$ (**A**), strong interaction, $|H_{ab}|/\lambda \geq 0.5$ (**B**), and moderate interaction, $|H_{ab}|/\lambda < 0.5$ (**C**). Bar plots represent hole distribution in the ground (gold yellow) and vertically excited (light yellow) states at the positions of global minima $x_{\min}$ on the ground adiabatic state.

The mixing coefficients $c_{i1}$ for the ground $\Psi_1$ and $c_{i2}$ for the excited $\Psi_2$ adiabatic states along with the corresponding energies $G_1$ and $G_2$ can be obtained by diagonalization of the $2 \times 2$ effective Hamiltonian matrix:

$$\mathbf{H} = \begin{bmatrix} G_a & H_{ab} \\ H_{ab} & G_b \end{bmatrix} = \begin{bmatrix} \lambda x^2 & H_{ab} \\ H_{ab} & \lambda(1-x)^2 \end{bmatrix}, \quad \text{(Eq. S4a)}$$

$$\mathbf{G} = \mathbf{\Psi}^{-1}\mathbf{H}\mathbf{\Psi} = \begin{bmatrix} G_1 & 0 \\ 0 & G_2 \end{bmatrix}, \quad \text{(Eq. S4b)}$$

where the diagonal elements of $\mathbf{H}$ are the diabatic state energies, and the off-diagonal elements $H_{ab} < 0$ are the coupling elements. These coupling elements $H_{ab}$ that describe the strength of the electronic interaction between the two units are considered to be independent of the coordinate $x$. Number of parameters in the parabolic model can be reduced to one by using $\lambda$ as an energy measurement unit. Indeed, dividing both sides of Equation S4 by $\lambda$ does not change the adiabatic state composition of $\Psi$, while the coupling elements and energies of diabatic and adiabatic states become simply scaled by $\lambda$:

$$\mathbf{H}/\lambda = \begin{bmatrix} x^2 & H_{ab}/\lambda \\ H_{ab}/\lambda & (1-x)^2 \end{bmatrix}, \quad \text{(Eq. S5a)}$$

$$\mathbf{G}/\lambda = \mathbf{\Psi}^{-1}(\mathbf{H}/\lambda)\mathbf{\Psi} = \begin{bmatrix} G_1/\lambda & 0 \\ 0 & G_2/\lambda \end{bmatrix}. \quad \text{(Eq. S5b)}$$

The resulting ground-state energy is lowered relative to the original diabatic states, whereas the excited-state energy is increased:

$$G_1 = \frac{1}{2}\left\{ (G_b + G_a) - \sqrt{(G_b - G_a)^2 + 4H_{ab}^2} \right\},$$
$$G_2 = \frac{1}{2}\left\{ (G_b + G_a) + \sqrt{(G_b - G_a)^2 + 4H_{ab}^2} \right\}, \quad \text{(Eq. S6)}$$

which gives the energy curves for these states in terms of the parabolic diabatic states and the charge-transfer coordinate $x$:

$$G_1(x)/\lambda = \frac{1}{2}\left\{ (2x^2 - 2x + 1) - \sqrt{(1-2x)^2 + 4(H_{ab}/\lambda)^2} \right\},$$
$$G_2(x)/\lambda = \frac{1}{2}\left\{ (2x^2 - 2x + 1) + \sqrt{(1-2x)^2 + 4(H_{ab}/\lambda)^2} \right\}. \quad \text{(Eq. S7)}$$

The distribution of the hole across the two units in the ground, $Q_1$, and excited, $Q_2$, adiabatic states can then be evaluated as squares of the coefficients $c_{ij}$ (Equation S8), each representing weight of the pure diabatic state $\psi_i$ in the mixed adiabatic state $\Psi_j$, and visualized with bar plots (Figure S25).

$$Q_1 = \begin{bmatrix} c_{11}^2 \\ c_{21}^2 \end{bmatrix}, Q_2 = \begin{bmatrix} c_{12}^2 \\ c_{22}^2 \end{bmatrix}. \quad \text{(Eq. S8)}$$

Importantly, adiabatic states $\Psi_j$ are orthonormal, i.e. sum of $c_{ij}^2$ for each adiabatic state is equal to one, so the hole is normalized.

Depending on the coupling strength $H_{ab}$ between the diabatic states, three regimes of the hole localization are possible, as shown in Figure S25.[24b] In the case of very weak coupling ($|H_{ab}|/\lambda \approx 0$) the resulting adiabatic states are almost identical to the original diabatic states:

$$\Psi_1 \approx \psi_a = \begin{bmatrix} 1 \\ 0 \end{bmatrix}, \Psi_2 \approx \psi_b = \begin{bmatrix} 0 \\ 1 \end{bmatrix}, \qquad x < 0.5,$$

$$\Psi_1 \approx \psi_b = \begin{bmatrix} 0 \\ 1 \end{bmatrix}, \Psi_2 \approx \psi_a = \begin{bmatrix} 1 \\ 0 \end{bmatrix}, \qquad x > 0.5. \qquad \text{(Eq. S9)}$$

The hole position, determined by a minimum on the ground state energy curve, is in this case on a single unit, at $x \approx 0$ or 1. The energy required to transfer the hole to another unit $\Delta G^{\neq}$ is then approximately equal to $\lambda/4$, and the vertical excitation energy $\Delta G_{1\rightarrow 2}$ is equal to $\lambda$ (Figure S25).

On the other hand, if the coupling is very strong ($|H_{ab}|/\lambda \geq 0.5$), it gives rise to single-well adiabatic ground and excited states, where the hole is equally shared between the two units, with the energy minimum at $x = 0.5$ (Figure S25B). The ground state then becomes an equal mixture of the two diabatic states:

$$\Psi_1 = \tfrac{1}{\sqrt{2}}\psi_a + \tfrac{1}{\sqrt{2}}\psi_b = \tfrac{1}{\sqrt{2}} \begin{bmatrix} 1 \\ 1 \end{bmatrix},$$

$$\Psi_2 = \tfrac{1}{\sqrt{2}}\psi_a - \tfrac{1}{\sqrt{2}}\psi_b = \tfrac{1}{\sqrt{2}} \begin{bmatrix} 1 \\ -1 \end{bmatrix}. \qquad \text{(Eq. S10)}$$

In this case, the vertical excitation energy equals to twice the coupling element, $\Delta G_{1\rightarrow 2} = 2|H_{ab}|$.

In the intermediate regime ($|H_{ab}|/\lambda < 0.5$), the two diabatic states couple giving rise to a two-minima ground adiabatic state and a single-minimum excited state (Figure S25C). In this case, at the ground state minimum $x_{min}$ the ground and excited states are unequal mixtures of the diabatic states, e.g. $c_{11} > c_{21}$ and $c_{12} < c_{22}$ (Equation S3). Thus, the hole is only partially localized on one of the units, and its redistribution requires activation energy $[(\lambda - 2|H_{ab}|)^2/4\lambda]$, whereas the vertical excitation energy is simply $\lambda$.

## S8. Multi-state parabolic model

In the simplest case that corresponds to $^{H}\mathbf{PP}_n^{+\bullet}$ series where we can assume that all units are equivalent [25], the extended Hamiltonian can be written as:

$$\mathbf{H} = \lambda \begin{bmatrix} x^2 & H_{ab}/\lambda & . & 0 & 0 \\ H_{ab}/\lambda & (1-x)^2 & . & H_{ab}/\lambda & 0 \\ . & . & \cdots & . & . \\ 0 & H_{ab}/\lambda & . & (n-2-x)^2 & H_{ab}/\lambda \\ 0 & 0 & . & H_{ab}/\lambda & (n-1-x)^2 \end{bmatrix} \qquad \text{(Eq. S11)}$$

Here, we take all couplings between adjacent parabolas (sub- and super-diagonal elements of the effective Hamiltonian in Equation S11) to be equal, and all other couplings to be zero, so the generalized Hamiltonian depends only on one parameter $H_{ab}/\lambda$. Similar to the two-parabolic model, adiabatic state compositions and energies can be obtained by diagonalizing the Hamiltonian:

$$\begin{matrix} \quad \Psi_1 \quad \Psi_2 \quad . \quad \Psi_n \\ \mathbf{\Psi} = \begin{bmatrix} c_{11} & c_{12} & . & c_{1n} \\ c_{21} & c_{22} & . & c_{2n} \\ . & . & \cdots & . \\ c_{n1} & c_{n2} & . & c_{nn} \end{bmatrix}, Q_j = \begin{bmatrix} c_{1j}^2 \\ c_{2j}^2 \\ \cdots \\ c_{nj}^2 \end{bmatrix}, \end{matrix} \qquad \text{(Eq. S12a)}$$

$$\mathbf{G}/\lambda = \mathbf{\Psi}^{-1}(\mathbf{H}/\lambda)\mathbf{\Psi} = \begin{bmatrix} G_1/\lambda & 0 & . & 0 \\ 0 & G_2/\lambda & . & 0 \\ . & . & \cdots & . \\ 0 & 0 & . & G_n/\lambda \end{bmatrix} \qquad \text{(Eq. S12b)}$$
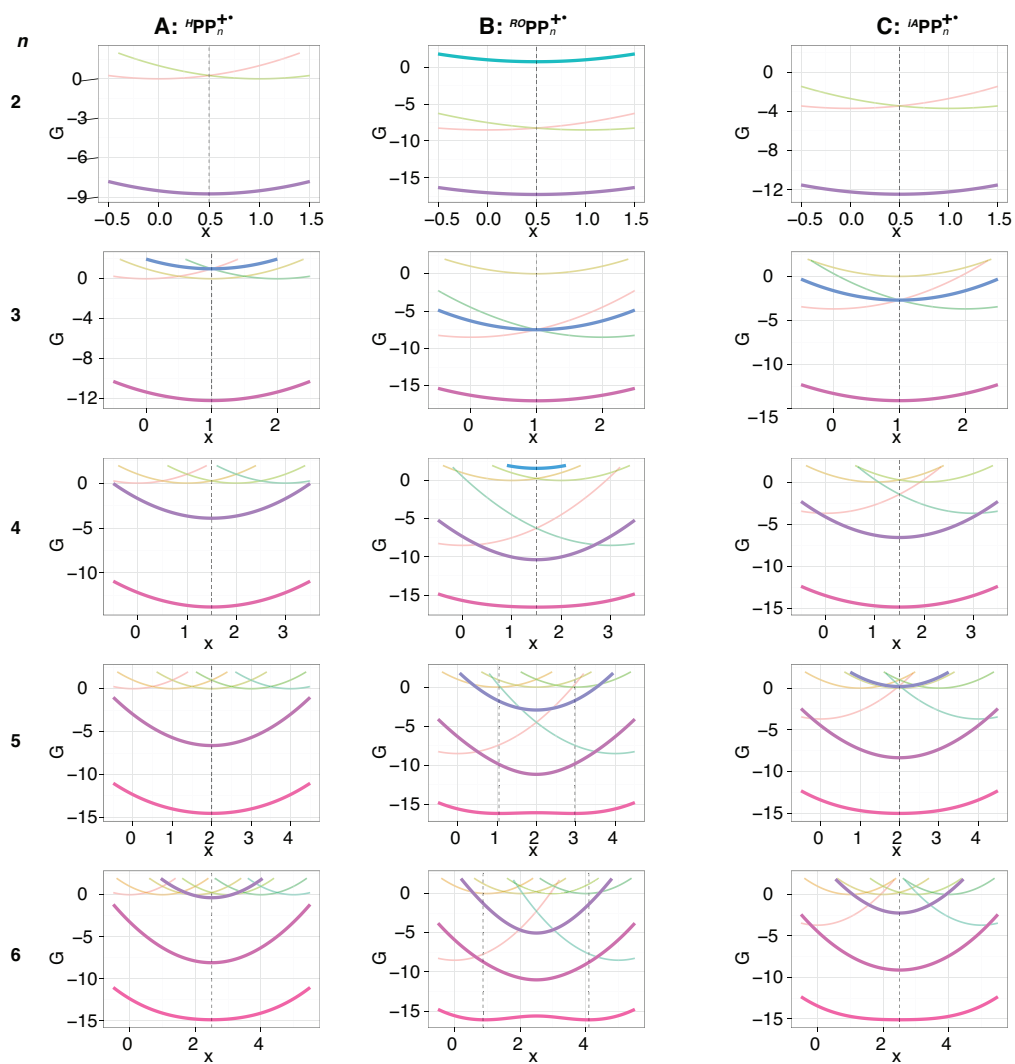
**Figure S26**. Ground and first excited states of various $^{R}\mathrm{PP}_{n}^{+\bullet}$ series, $n = 2\text{–}6$: $^{H}\mathrm{PP}_{n}^{+\bullet}$, $\Delta\varepsilon/\lambda = 0$ (**A**); $^{RO}\mathrm{PP}_{n}^{+\bullet}$, $\Delta\varepsilon/\lambda = 8.5$ (**B**); $^{iA}\mathrm{PP}_{n}^{+\bullet}$, $\Delta\varepsilon/\lambda = 3.7$ (**C**), plotted along the hole transfer coordinate $x$. For all series, the constant value of $H_{ab}/\lambda = -9$ was used. Thin lines represent diabatic 'pure' states, and thick lines represent adiabatic 'mixed' states. The dashed line denotes positions of the minima.
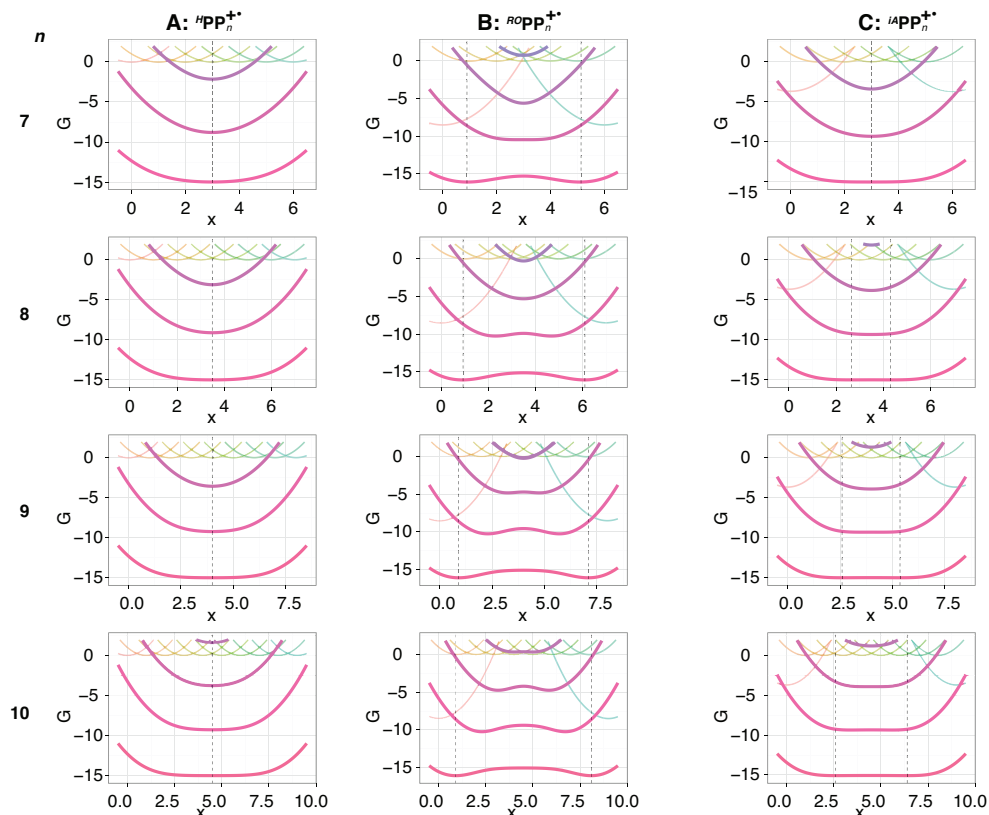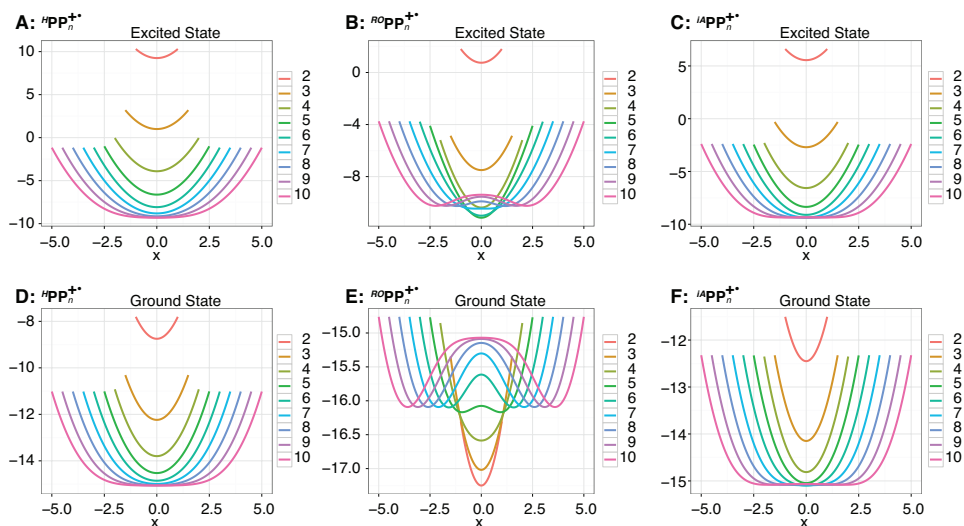
**Figure S27**. Ground and several excited states of various $^{R}\text{PP}_n^{+\bullet}$ series, $n = 7–10$: $^{H}\text{PP}_n^{+\bullet}$, $\Delta\varepsilon/\lambda = 0$ (**A**); $^{RO}\text{PP}_n^{+\bullet}$, $\Delta\varepsilon/\lambda = 8.5$ (**B**); $^{iA}\text{PP}_n^{+\bullet}$, $\Delta\varepsilon/\lambda = 3.7$ (**C**), plotted along the hole transfer coordinate $x$. For all series, the constant value of $H_{ab}/\lambda = -9$ was used. Thin lines represent diabatic 'pure' states, and thick lines represent adiabatic 'mixed' states. The dashed line denotes positions of the minima.



**Figure S28**. Ground and first excited adiabatic state curves corresponding to $^{H}\text{PP}_n^{+\bullet}$, $\Delta\varepsilon/\lambda = 0$ (**D, A**); $^{RO}\text{PP}_n^{+\bullet}$, $\Delta\varepsilon/\lambda = 8.5$ (**E, B**); $^{iA}\text{PP}_n^{+\bullet}$, $\Delta\varepsilon/\lambda = 3.7$ (**F, C**). Thin lines represent diabatic 'pure' states, and thick lines represent adiabatic 'mixed' states.
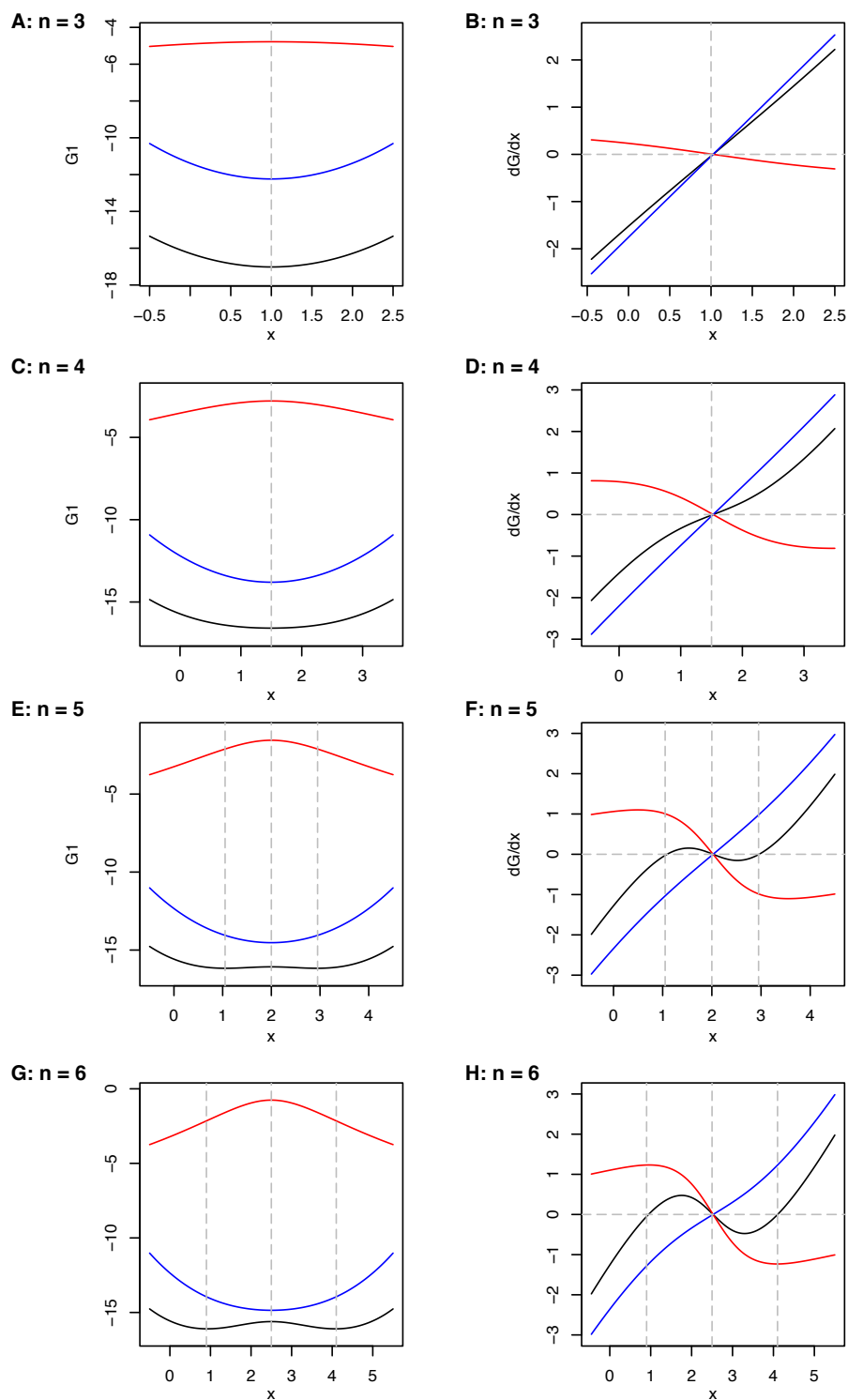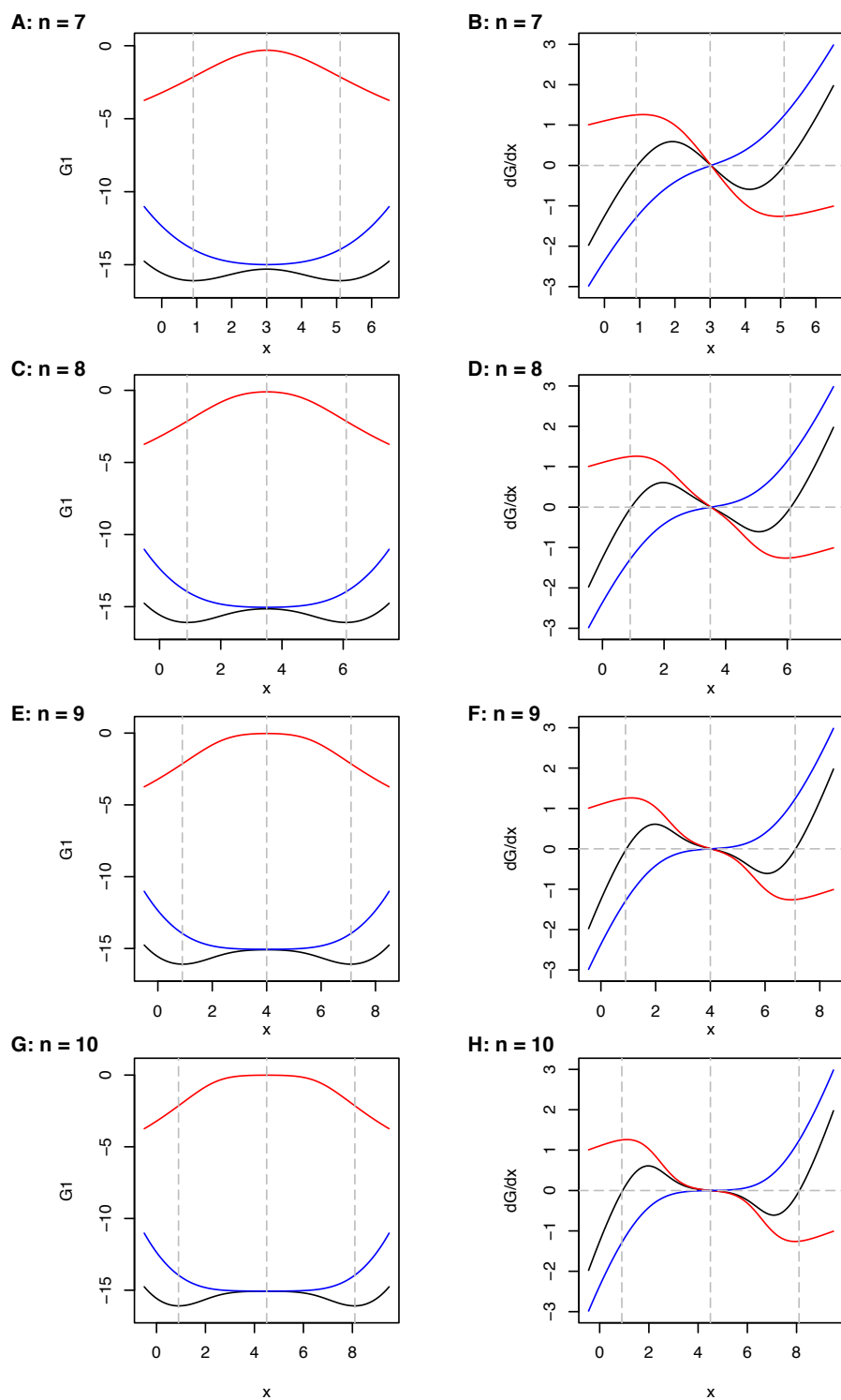
**Figure S29**. Left column: adiabatic ground state curves for the $^{RO}PP_n^{+\bullet}$ models, $n = 3$–$6$ (black lines); delocalization component of the adiabatic curves (blue lines), and the effect of terminal units on the adiabatic curves (red lines). Right column: Derivatives of the aforementioned curves with respect to the reaction coordinate $x$, which can be interpreted as forces acting on the hole. Dominant components of the total force are shown in solid (blue or red) lines, while lesser contributors are depicted by dashed line. $H_{ab}/\lambda = 9$, $\Delta\varepsilon/\lambda = 8.5$.
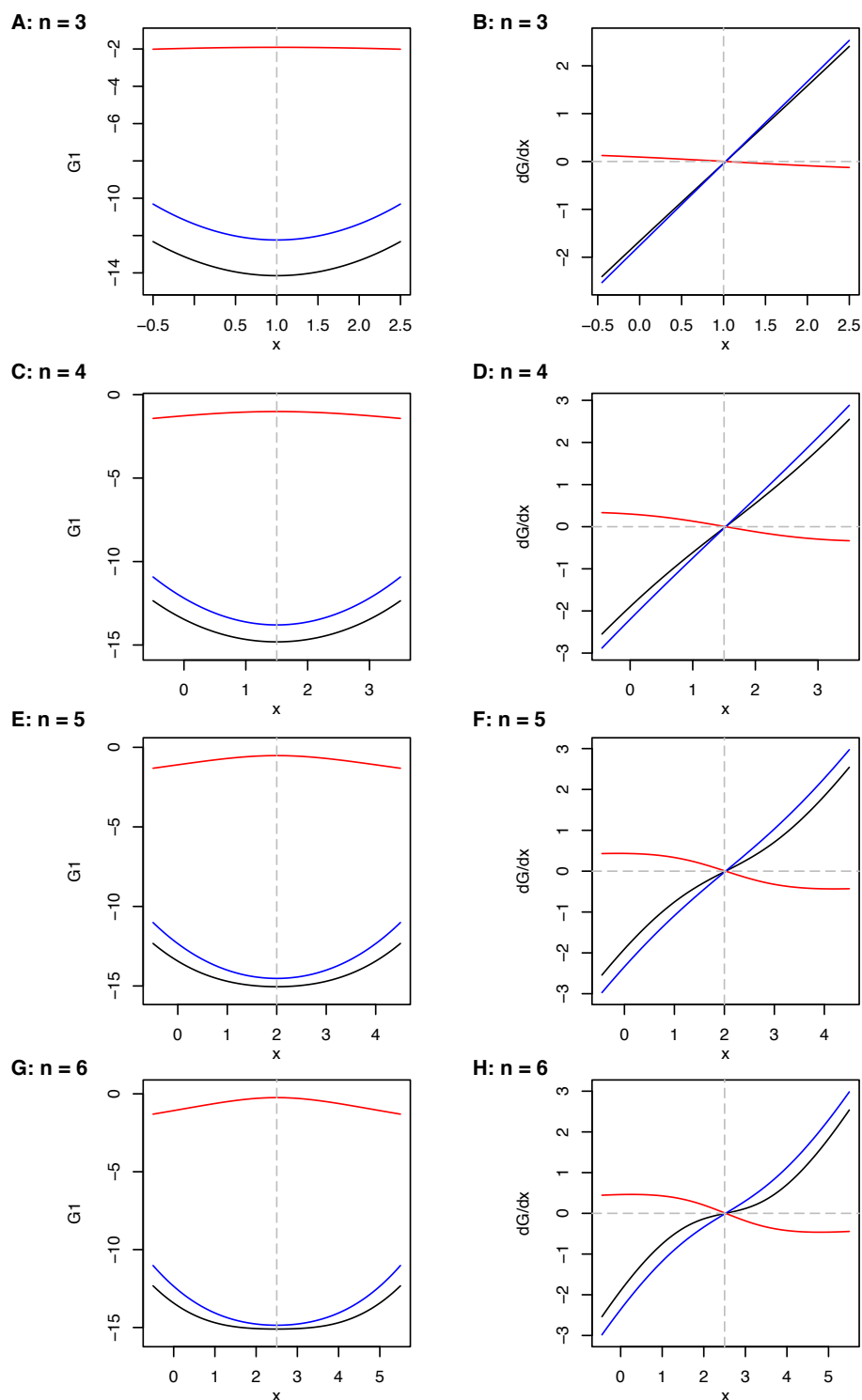
**Figure S30**. Left column: adiabatic ground state curves for the $^{RO}\mathbf{PP}_n^{+\bullet}$ models, $n$ = 7–10 (black lines); delocalization component of the adiabatic curves (blue lines), and the effect of terminal units on the adiabatic curves (red lines). Right column: Derivatives of the aforementioned curves with respect to the reaction coordinate $x$, which can be interpreted as forces acting on the hole. Dominant components of the total force are shown in solid (blue or red) lines, while lesser contributors are depicted by dashed line. $H_{ab}/\lambda = -9$, $\Delta\varepsilon/\lambda = 8.5$.

**Figure S31**. Left column: adiabatic ground state curves for the $^{iA}PP_n^{+\bullet}$ models, $n = 3–6$ (black lines); delocalization component of the adiabatic curves (blue lines), and the effect of terminal units on the adiabatic curves (red lines). Right column: Derivatives of the aforementioned curves with respect to the reaction coordinate $x$, which can be interpreted as forces acting on the hole. Dominant components of the total force are shown in solid (blue or red) lines, while lesser contributors are depicted by dashed line. $H_{ab}/\lambda = -9$, $\Delta\varepsilon/\lambda = 3.7$.
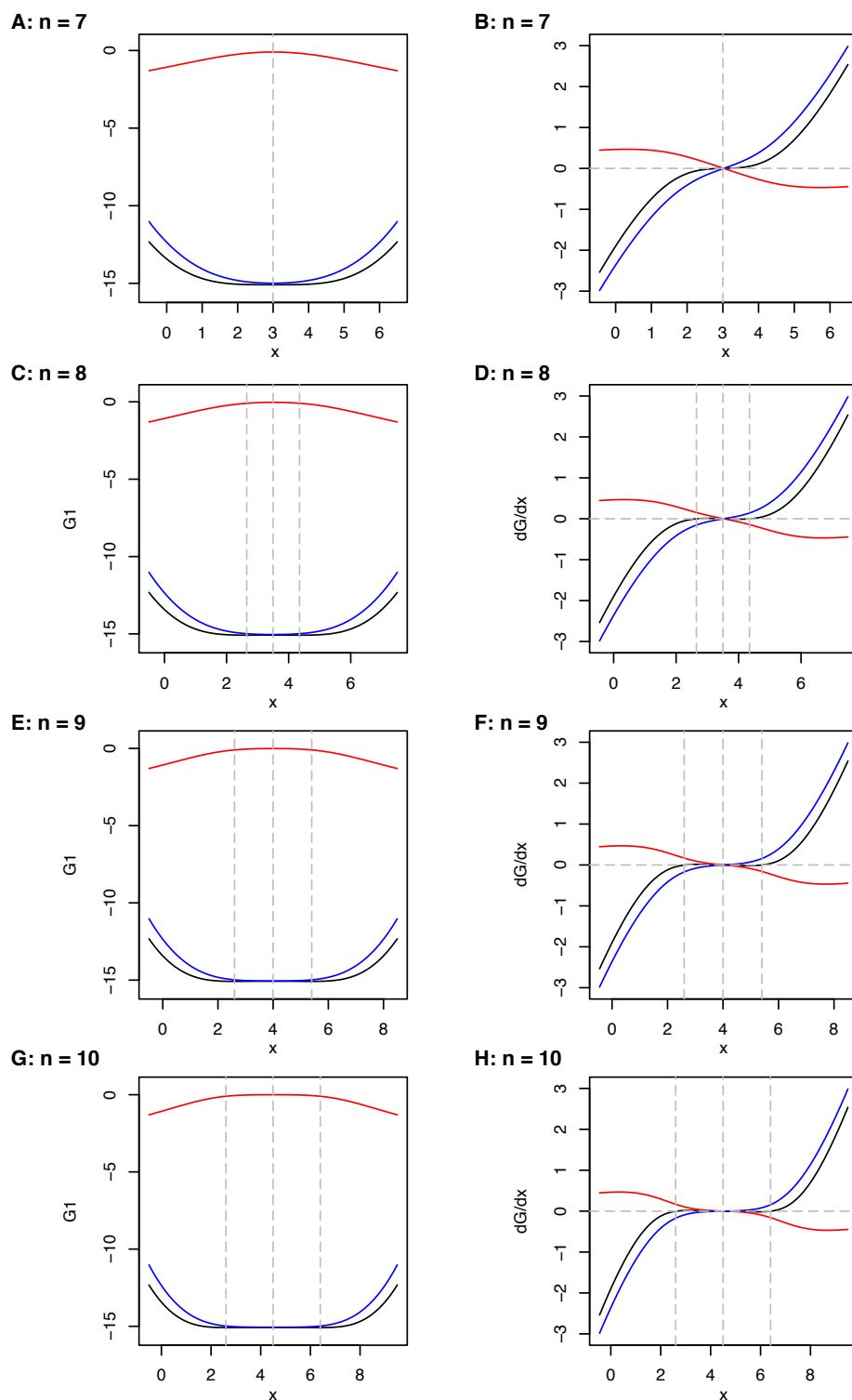
**Figure S32**. Left column: adiabatic ground state curves for the $^{i4}\mathbf{PP}_n^{+\bullet}$ models, $n$ = 7–10 (black lines); delocalization component of the adiabatic curves (blue lines), and the effect of terminal units on the adiabatic curves (red lines). Right column: Derivatives of the aforementioned curves with respect to the reaction coordinate $x$, which can be interpreted as forces acting on the hole. Dominant components of the total force are shown in solid (blue or red) lines, while lesser contributors are depicted by dashed line. $H_{ab}/\lambda = -9$, $\Delta\varepsilon/\lambda = 3.7$.

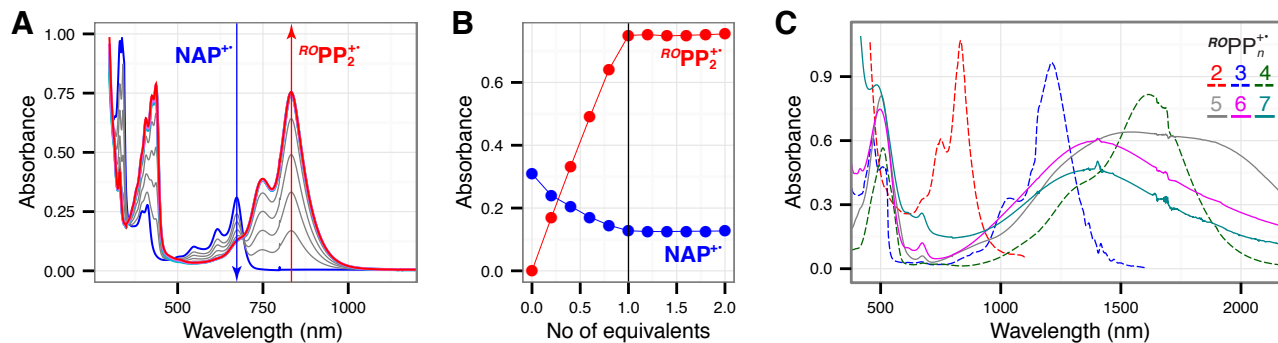## S9.  Coexistence of the two forms of $^{RO}$PP$_5^{+\bullet}$



**Figure S33**. (**A**) Spectral changes upon the reduction of 0.1 mM naphthalene cation radical by an incremental addition of 0.77 mM solution of $^{RO}$**PP$_2$** in dichloromethane at 20 $^\circ$C (25 μL increment). (**B**) A plot of increase of the absorbance of $^{RO}$**PP$_2^{+\bullet}$** (monitored at 832 nm), and depletion of the absorbance of naphthalene cation radical **NAP$^{+\bullet}$** (monitored at 672 nm) against the equivalent of added $^{RO}$**PP$_2$**. (**C**) A comparison of the cation radical spectra of various $^{RO}$**PP$_n^{+\bullet}$**, generated similarly, in dichloromethane at 20 $^\circ$C.
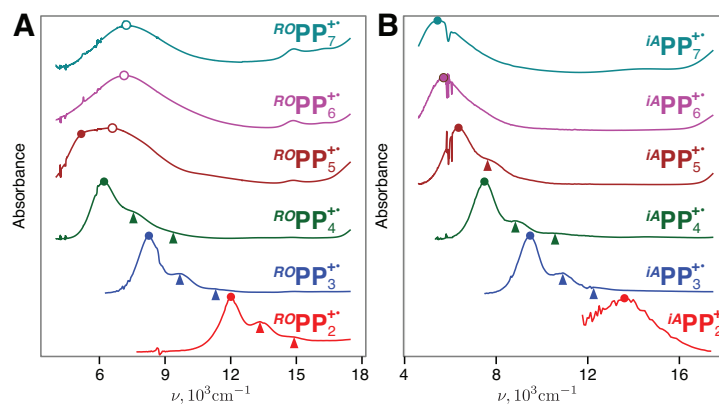


**Figure S34**. Absorption spectra of $^{RO}$**PP$_n^{+\bullet}$** (**A**) obtained in as well as the $^{iA}$**PP$_n^{+\bullet}$** spectra from Ref. 14 (Ref. 4a of the main text) given for comparison (**B**). Solvent: dichloromethane, 20 ºC. Filled circles and triangles denote absorption maxima and corresponding vibronic progressions for CRs, in which hole is likely distributed in the middle of the chain. The separation between vibronic peaks, ~1300 cm$^{-1}$ (which is similar to that in the emission spectra of $^{iA}$**PP$_n$** and absorption spectra of $^{iA}$**PP$_n^{+\bullet}$**),[14,26] suggests that the band corresponds to the backbone C–C bond vibrations. Open circles denote absorption maxima of CRs in which the hole is presumably distributed near an end of the chain.
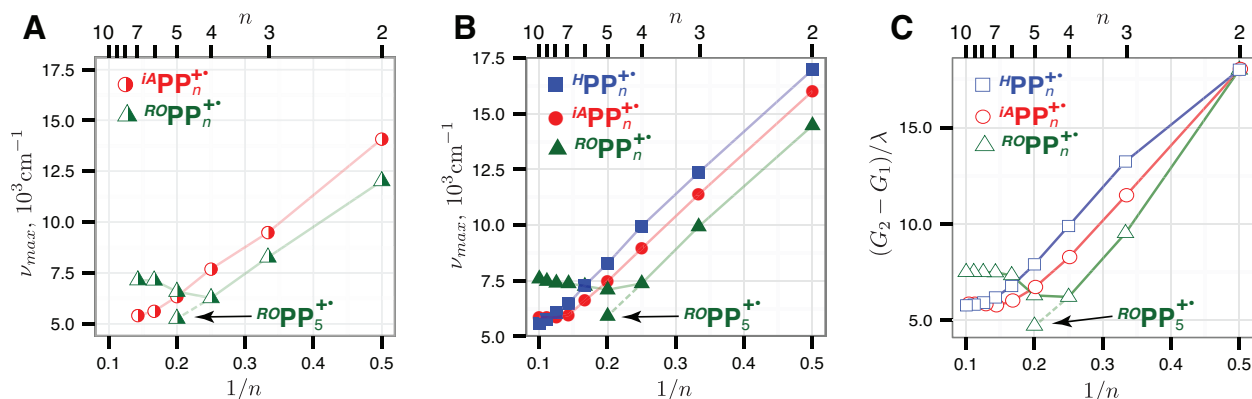
**Figure S35**. Vertical excitation energies of various $^{R}\mathbf{PP}_n^{+\bullet}$, obtained from the experimental absorption spectra (**A**), from TD-DFT calculations (**B**), and from the multi-state parabolic model (**C**). In panel (**A**), positions of two points for $^{RO}\mathbf{PP}_5^{+\bullet}$ correspond to the positions of two peaks that comprise a broad near-infrared absorption band for $^{RO}\mathbf{PP}_5^{+\bullet}$ (see Figures 2C and S34 for actual spectra). In panels **B** and **C**, upper point for $^{RO}\mathbf{PP}_5^{+\bullet}$ corresponds to the minimum on energetic profile, in which hole is displaced towards the end of the chain, while the lower point corresponds to a higher-energy form (by 0.3 kcal/mol, B1LYP-40 calculations) with the hole symmetrically distributed in the middle of the chain.
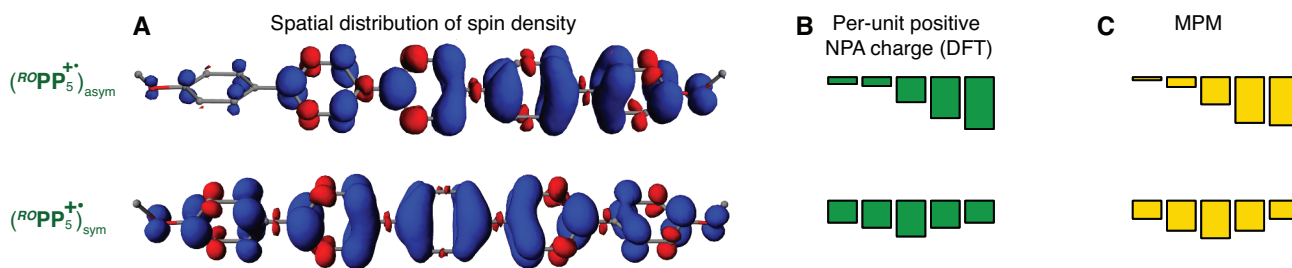


**Figure S36**. Ground state hole distribution at the minimum on the potential energy surface of $^{RO}\mathbf{PP}_5^{+\bullet}$, in which hole is displaced towards the end of the chain (top), and the saddle point, in which hole is symmetrically distributed in the middle of the chain (bottom). Isosurface plots show spatial distribution of the unpaired spin density (**A**); green-colored bar charts represent condensed per-unit positive charge $\Delta q^+$, calculated with natural population analysis (**B**), and yellow-colored bar charts represent hole distribution as calculated by the multi-state parabolic model (**C**).

## S10.　　　　References

(1) Frisch, M. J.; Trucks, G. W.; Schlegel, H. B.; Scuseria, G. E.; Robb, M. A.; Cheeseman, J. R.; Scalmani, G.; Barone, V.; Mennucci, B.; Petersson, G. A.; Nakatsuji, H.; Caricato, M.; Li, X.; Hratchian, H. P.; Izmaylov, A. F.; Bloino, J.; Zheng, G.; Sonnenberg, J. L.; Hada, M.; Ehara, M.; Toyota, K.; Fukuda, R.; Hasegawa, J.; Ishida, M.; Nakajima, T.; Honda, Y.; Kitao, O.; Nakai, H.; Vreven, T.; Montgomery, J. A.; Peralta, J. E.; Ogliaro, F.; Bearpark, M.; Heyd, J. J.; Brothers, E.; Kudin, K. N.; Staroverov, V. N.; Kobayashi, R.; Normand, J.; Raghavachari, K.; Rendell, A.; Burant, J. C.; Iyengar, S. S.; Tomasi, J.; Cossi, M.; Rega, N.; Millam, J. M.; Klene, M.; Knox, J. E.; Cross, J. B.; Bakken, V.; Adamo, C.; Jaramillo, J.; Gomperts, R.; Stratmann, R. E.; Yazyev, O.; Austin, A. J.; Cammi, R.; Pomelli, C.; Ochterski, J. W.; Martin, R. L.; Morokuma, K.; Zakrzewski, V. G.; Voth, G. A.; Salvador, P.; Dannenberg, J. J.; Dapprich, S.; Daniels, A. D.; Farkas; Foresman, J. B.; Ortiz, J. V.; Cioslowski, J.; Fox, D. J.  Gaussian, Inc., Wallingford CT, 2009.
(2) Adamo, C.; Barone, V. *Chem. Phys. Lett.* **1997**, *274*, 242-250.
(3) Hehre, W. J.; Ditchfield, R.; Pople, J. A. *J. Chem. Phys.* **1972**, *56*, 2257-2261.
(4) (a) Cances, M. T.; Mennucci, V.; Tomasi, J. *J. Chem. Phys.* **1997**, *107*, 3032-3041; (b) Cossi, M.; Barone, V.; Mennucci, V.; Tomasi, J. *Chem. Phys. Lett* **1998**, *286*, 253-260; (c) Miertus, S.; Scrocco, E.; Tomasi, J. *Chem. Phys.* **1981**, *55*, 117-117; (d) Tomasi, J.; Mennucci, B.; Cammi, R. *Chem. Rev. (Washington, DC, U. S.)* **2005**, *105*, 2999-3093; (e) Ribeiro, R. F.; Marenich, A. V.; Cramer, C. J.; Truhlar, D. G. *J. Phys. Chem. B* **2011**, *115*, 14556-14562.
(5) (a) Bauernschmitt, R.; Ahlrichs, R. *J. Chem. Phys.* **1996**, *104*, 9047-9052; (b) Seeger, R.; Pople, J. A. *J. Chem. Phys.* **1977**, *66*, 3045-3050.
(6) Reed, A. E.; Curtiss, L. A.; Weinhold, F. *Chem. Rev. (Washington, DC, U. S.)* **1988**, *88*, 899-926.
(7) Weinhold, F.; Landis, C. R. *Valency and Bonding: A Natural Bond Orbital Donor-Acceptor Perspective*; Cambridge University Press: Cambridge, U.K., 2005.
(8) (a) Bauernschmitt, R.; Ahlrichs, R. *Chem. Phys. Lett.* **1996**, *256*, 454-464; (b) Casida, M. E.; Jamorski, C.; Casida, K. C.; Salahub, D. R. *J. Chem. Phys.* **1998**, *108*, 4439-4449; (c) Stratmann, R. E.; Scuseria, G. E.; Frisch, M. J. *J. Chem. Phys.* **1998**, *109*, 8218-8224; (d) Cammi, R.; Mennucci, B.; Tomasi, J. *The Journal of Physical Chemistry A* **2000**, *104*, 5631-5637; (e) Cossi, M.; Barone, V. *J. Chem. Phys.* **2001**, *115*, 4708-4717.
(9) Wiberg, K. B.; Hadad, C. M.; LePage, T. J.; Breneman, C. M.; Frisch, M. J. *J. Phys. Chem.* **1992**, *96*, 671-679.
(10) (a) Cohen, A. J.; Mori-Sanchez, P.; Yang, W. *Science* **2008**, *321*, 792-794; (b) Renz, M.; Theilacker, K.; Lambert, C.; Kaupp, M. *J. Am. Chem. Soc.* **2009**, *131*, 16292-302; (c) Cohen, A. J.; Mori-Sanchez, P.; Yang, W. *Chem. Rev. (Washington, D. C.)* **2012**, *112*, 289-320.
(11) A removal of one electron from a neutral donor produces a cation radical which was coined in the term 'hole' by N. Bauld. In this study, the use of term hole also encompasses reorganization of electron density, structural and solvent rearrangements.
(12) (a) Dierksen, M.; Grimme, S. *J. Phys. Chem. A* **2004**, *108*, 10225-10237; (b) Félix, M.; Voityuk, A. A. *Int. J. Quantum Chem.* **2011**, *111*, 191-201.
(13) (a) Renz, M.; Kess, M.; Diedenhofen, M.; Klamt, A.; Kaupp, M. *J. Chem. Theory Comput.* **2012**, *8*, 4189-4203; (b) Yang, J.; Zhang, W.; Si, Y.; Zhao, Y. *J. Phys. Chem. B* **2012**, *116*, 14126-14135.
(14) Banerjee, M.; Shukla, R.; Rathore, R. *J. Am. Chem. Soc.* **2009**, *131*, 1780-1786.
(15) (a) Becke, A. D. *Phys. Rev. A: Gen. Phys.* **1988**, *38*, 3098; (b) Lee, C.; Yang, W.; Parr, R. G. *Phys. Rev. B: Condens. Matter* **1988**, *37*, 785.
(16) (a) Becke, A. D. *J. Chem. Phys.* **1993**, *98*, 5648-5648; (b) Stephens, P. J.; Devlin, F. J.; Chabalowski, C. F.; Frisch, M. J. *J. Phys. Chem.* **1994**, *98*, 11623.
(17) Yanai, T.; Tew, D. P.; Handy, N. C. *Chem. Phys. Lett.* **2004**, *393*, 51.
(18) Iikura, H.; Tsuneda, T.; Yanai, T.; Hirao, K. *J. Chem. Phys.* **2001**, *115*, 3540-3544.
(19) Zhao, Y.; Truhlar, D. G. *Theor. Chem. Acc.* **2008**, *120*, 215-241.
(20) Zhao, Y.; Truhlar, D. G. *J. Phys. Chem. A* **2006**, *110*, 13126-13130.
(21) Chai, J. D.; Head-Gordon, M. *J. Chem. Phys.* **2008**, *128*, 084106.
(22) Chai, J. D.; Head-Gordon, M. *Phys. Chem. Chem. Phys.* **2008**, *10*, 6615-20.
(23) Rathore, R.; Burns, C. L.; Deselnicu, M. I. *Org. Lett.* **2001**, *3*, 2887-2890.
(24) (a) Hush, N. S. *Prog. Inorg. Chem.* **1967**, *8*, 391-444; (b) Robin, M. B.; Day, P. *Advan. Inorg. Chem. Radiochem.* **1967**, *10*, 247-422; (c) Marcus, R. A.; Sutin, N. *Biochim. Biophys. Acta, Rev. Bioenerg.* **1985**, *811*, 265-322; (d) Brunschwig, B. S.; Creutz, C.; Sutin, N. *Chem. Soc. Rev.* **2002**, *31*, 168-184.
(25) In the case of $^{n}$**PP**$_{n}$ cation radicals , the terminal phynelene units are slightly less efficient in stabilizing the hole and thus the corresponding parabolas should be somewhat shifted up relative to the internal units. However, this effect is expected to

be marginally small, especially considering that for the longer chains the hole stabilization is dominated by the bridging internal units.

(26) Heimel, G.; Daghofer, M.; Gierschner, J.; List, E. J. W.; Grimsdale, A. C.; Müllen, K.; Beljonne, D.; Brédas, J.-L.; Zojer, E. *J. Chem. Phys.* **2005**, *122*, 54501.